

University Degree in Biomedical Engineering  
2023-2024

*Bachelor Thesis*

“Severity Score Assignment by Artificial  
Intelligence Segmentation Tools for  
Prediction of Vasospasm in  
Subarachnoid Hemorrhage Patients”

---

Elena Martínez Torrijos

Matilde Pilar Sánchez Fernández  
José Ángel Lorente Balanza  
Leganés, June 2024



This work is licensed under Creative Commons **Attribution – Non Commercial – Non Derivatives**



## SUMMARY

*Background and Motivation:* This bachelor thesis explores the potential of artificial intelligence (AI) in risk stratification of patients with aneurysmal subarachnoid hemorrhage (aSAH). aSAH is an acute cerebrovascular condition that can lead to severe complications such as vasospasm, which is presented as a focal neurological deficit. Despite the existence of various grading scales for assessing vasospasm risk, such as the modified Fisher scale, accurately predicting vasospasm remains a significant challenge. The pertinence of this project was ensured by a systematic review conducted between September and December 2023.

*Objectives:* The aim of this project is to automate the process of assigning the modified Fisher scale to aSAH patients, and to integrate this scale with other baseline and CT features to enhance the prediction of vasospasm. Secondary objectives include the design of an accurate hemorrhage segmentation model (from which volume, density, thickness and localization measurements are computed) and the variability analysis between the modified Fisher Scale assignment of two neuroradiologists.

*Methods:* Five different image segmentation techniques were evaluated. Two different classifiers were designed for the automated assessment of the modified Fisher Scale and the vasospasm prediction.

*Results:* The U-Net segmentation model achieved a Dice score of 95%, resulting in a precise differentiation of the hemorrhage and enabling accurate feature computation.

Regarding the modified Fisher classifier, the model was able to successfully assign higher risk of vasospasm - grade 4 (mean ROC AUC of  $0.95 \pm 0.08$ ), moderate risk of vasospasm - grades 2 and 3 (mean ROC AUC of  $0.80 \pm 0.13$ ) and lower risk of vasospasm - grades 0 and 1 (mean ROC AUC of  $0.89 \pm 0.10$ ). It displayed a moderate Kappa coefficient of 0.54 when compared to manual measurements.

The model for vasospasm prediction yielded a mean ROC AUC of  $0.69 \pm 0.16$ , outperforming the predictive capacity of current risk scales used in clinical practice. Input features for this model included hemorrhage volume and thickness, the modified Fisher scale and patient's age.

*Conclusion:* This project establishes the foundation for future approaches, fulfilling the stated objectives of the new AI-model for modified Fisher assignment and the extended scale for vasospasm prediction. Further studies should explore more sophisticated AI methods to keep enhancing outcomes in this field.

**Keywords:** Artificial intelligence (AI), aneurysmal subarachnoid hemorrhage (aSAH), vasospasm, delayed cerebral ischemia (DCI), modified Fisher scale, image segmentation, CT scan.

# Visual Abstract

Severity Score assignment by artificial intelligence (AI) segmentation tools for prediction of vasospasm in subarachnoid hemorrhage (SAH) patients

## OBJECTIVES

1. Segmentation model development
2. Automatically assign the modified Fisher scale
3. Interobserver variability assessment
4. Predictive evaluation of vasospasm
5. NEW SCALE for vasospasm prediction

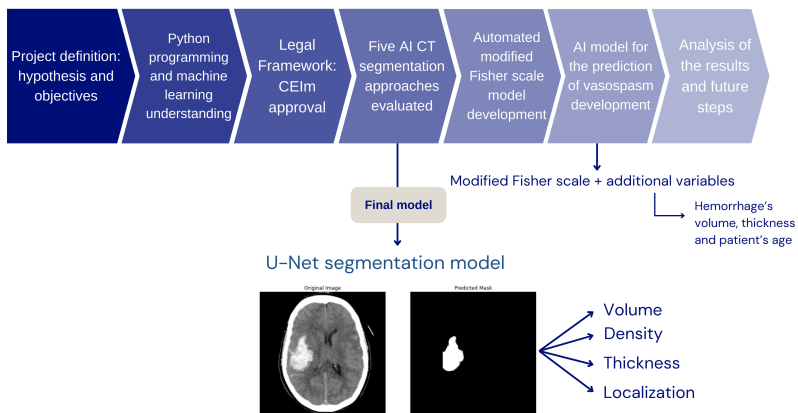
## Study subjects

n = 143 SAH patients from Hospital Universitario de Getafe

## Theoretical background

Systematic Review of >140 articles

## METHODS

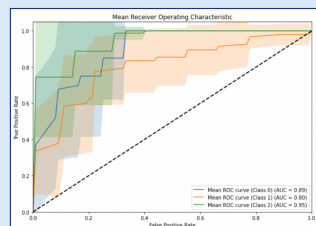


## RESULTS

### 1 Segmentation Model

Dice Score = 95%

### 2 AI-Modified Fisher



- Highest risk of vasospasm (grade 4): AUC = 0.95
- Intermediate risk of vasospasm (grades 3 and 2): AUC = 0.80
- Low risk of vasospasm (grades 1 and 0): AUC = 0.89

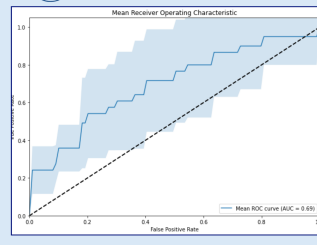
### 3 Interobserver variability

Kappa coefficient = 0.95

### 4 Model's predictive evaluation

Highest grade: sensitivity = 80%, specificity = 16.67%

### 5 Vasospasm model



Vasospasm prediction: AUC = 0.69

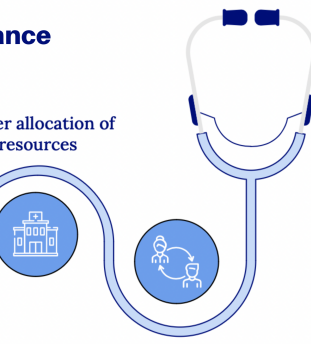
## Clinical Relevance

Improve SAH patients outcomes

Better allocation of resources

Early diagnosis

↓ interobserver variability in modified Fisher scale





## **ACKNOWLEDGMENTS AND DEDICATION**

I would like to express my deepest gratitude to my thesis tutors, Dr. José Ángel Lorente Balanza and Matilde Pilar Sánchez Fernández, for their invaluable guidance and support throughout this journey. Their expertise and encouragement have been crucial to my academic and personal growth. My sincere thanks also go to Pablo Martínez Olmos, Dr. Jorge Mario Sánchez, and Dr. Eva Tejerina for their significant contributions and assistance. Through their mentorship, I have gained extensive knowledge and discovered a field of work that I am passionate about and will continue to pursue.

To my parents and role models, Ana and Nacho, for their constant effort in providing me with the best possible education and resources, while allowing me the freedom to follow my dreams. I am also deeply grateful to Lara and Bi for their essential support and encouragement.

To Marta, your companionship and understanding have been a constant source of inspiration. To Alejandro for his endless love, support, and patience. A big shoutout to my university friends Sofi, Elena, Ana, Clau, Lucía, Noelia, and Alex for making these four years full of laughter and unforgettable memories.

Finally, to my Lali, as all of my past, present, and future accomplishments are hers.



## CONTENTS

1. INTRODUCTION . . . . .	1
1.1. Aim and Motivation . . . . .	1
1.2. Subarachnoid Hemorrhage and Cerebral Vasospasm . . . . .	1
1.3. Clinical and Radiological Scores after aSAH . . . . .	4
1.4. Head Computed Tomography . . . . .	5
1.4.1. Houndsfield Units . . . . .	6
1.4.2. DICOM images . . . . .	7
1.5. Medical image segmentation . . . . .	8
1.5.1. U-Net . . . . .	9
1.6. Objectives . . . . .	10
1.6.1. Primary Objective . . . . .	10
1.6.2. Secondary Objectives . . . . .	11
1.7. Project Timeline . . . . .	11
2. STATE OF THE ART . . . . .	13
2.1. Systematic review . . . . .	13
2.1.1. No AI-Based Risk Scales . . . . .	13
2.1.2. AI-Based Risk Scales . . . . .	14
3. MATERIALS AND METHODS . . . . .	16
3.1. Study Design and Methodology . . . . .	16
3.2. Patient Population and Data Collection . . . . .	17
3.2.1. Modified Fisher Scale Assessment by Neuroradiologists . . . . .	18
3.3. Tools and Programming Environments Used . . . . .	18
3.4. Segmentation . . . . .	19
3.4.1. Thresholding-based Segmentation . . . . .	19
3.4.2. Automated Segmentation Models . . . . .	20
3.4.3. 3D Slicer Segmentation . . . . .	24
3.5. Segment Statistics . . . . .	24
3.5.1. Volume of the Segment . . . . .	24

3.5.2. Maximum Clot Thickness . . . . .	25
3.5.3. Hemorrhage Density . . . . .	25
3.5.4. Hemorrhage Localization . . . . .	25
3.6. Modified Fisher Scale Classifier . . . . .	26
3.6.1. Random Forest Classifier . . . . .	27
3.6.2. Logistic Regression Classifier. . . . .	27
3.7. Interobserver Variability and Model Comparison . . . . .	28
3.8. Vasospasm Classifiers . . . . .	29
4. ANALYSIS OF THE RESULTS . . . . .	30
4.1. Patient Population Results. . . . .	30
4.2. Segmentation Results and Final Model . . . . .	31
4.2.1. Thresholding-based Segmentation Results. . . . .	32
4.2.2. Automated Segmentation Models Results . . . . .	33
4.2.3. 3D Slicer Segmentation Results . . . . .	35
4.3. Segment Statistics Results. . . . .	37
4.4. Modified Fisher Scale Classifier Results . . . . .	37
4.4.1. Random Forest Classifier Results. . . . .	38
4.4.2. Logistic Regression Classifier Results . . . . .	40
4.5. Variability Results . . . . .	43
4.6. Vasospasm Classifiers Results . . . . .	44
4.6.1. Random Forest Classifier Results. . . . .	44
4.6.2. Logistic Regression Classifier Results . . . . .	45
5. DISCUSSION OF THE RESULTS . . . . .	47
5.1. Segmentation . . . . .	47
5.1.1. Thresholding-based Segmentation . . . . .	47
5.1.2. Automated Segmentation Models . . . . .	47
5.1.3. 3D Slicer Segmentation . . . . .	48
5.2. Segment Statistics . . . . .	49
5.3. Modified Fisher Scale Classifier . . . . .	50
5.3.1. Random Forest Classifier . . . . .	50
5.3.2. Logistic Regression Classifier. . . . .	51

5.4. Variability . . . . .	52
5.5. Vasospasm Classifiers . . . . .	52
5.6. Relevance of the Thesis . . . . .	53
5.7. Limitations and Possible Improvements . . . . .	53
6. REGULATORY FRAMEWORK . . . . .	54
7. SOCIOECONOMIC IMPACT . . . . .	55
7.1. Impact on the National Health System . . . . .	55
7.2. Project Resources . . . . .	55
7.2.1. Human Resources . . . . .	56
7.2.2. Material Resources . . . . .	56
7.2.3. Total Cost . . . . .	57
8. CONCLUSION AND FUTURE STEPS . . . . .	58
BIBLIOGRAPHY . . . . .	60



## LIST OF FIGURES

1.1	Meninges . . . . .	2
1.2	Schematic Illustration of an Aneurysm . . . . .	3
1.3	Digital Angiographic Cerebral Vasospasm . . . . .	4
1.4	SAH CT Image . . . . .	6
1.5	DICOM Hierarchy . . . . .	8
1.6	Segmentation Techniques . . . . .	9
1.7	Automated Blood Segmentation Results for a SAH Patient's Admission CT Scan . . . . .	9
1.8	U-Net Architecture . . . . .	10
1.9	Project Timeline . . . . .	12
3.1	Data Example . . . . .	18
3.2	MONAI Model Workflow . . . . .	21
3.3	Grid-based Localization of Hemorrhage . . . . .	26
4.1	Cohort Flowchart of aSAH Patients . . . . .	30
4.2	Thresholding-based Results. . . . .	32
4.3	U-Net Model Results 1 . . . . .	34
4.4	U-Net Model Results 2 . . . . .	34
4.5	U-Net Model Results 3 . . . . .	35
4.6	U-Net Model Results 4 . . . . .	35
4.7	Grow from Seeds Results . . . . .	36
4.8	Total Segmentator Results . . . . .	36
4.9	Hemorrhage Localization Results . . . . .	37
4.10	Binary Model Results . . . . .	38
4.11	Class Distribution with ADASYN . . . . .	39
4.12	Random Forest Classifier Results . . . . .	40
4.13	Class Distribution with SMOTE . . . . .	41
4.14	Logistic Regression Classifier Results . . . . .	42

4.15 Random Forest Classifier Results for Vasospasm . . . . .	44
4.16 Logistic Regression Classifier Results for Vasospasm . . . . .	45



## LIST OF TABLES

1.1	Main CT Scales for aSAH Evaluation. . . . .	5
3.1	Confusion Matrix . . . . .	27
4.1	ICU Database: Baseline characteristics, Severity Scales, Treatment and Complications of 143 aSAH patients. . . . .	31
4.2	Random Forest Confusion Matrix ( <i>mean ± std</i> ) . . . . .	40
4.3	Logistic Regression Confusion Matrix ( <i>mean ± std</i> ) . . . . .	42
4.4	Random Forest Confusion Matrix for Vasospasm ( <i>mean ± std</i> ) . . . . .	44
4.5	Random Forest Confusion Matrix for Vasospasm ( <i>mean ± std</i> ) . . . . .	45
7.1	Cost Breakdown of Human Resources . . . . .	56
7.2	Cost Breakdown of Material Resources . . . . .	57
7.3	Cost Breakdown of Total Resources . . . . .	57



## LIST OF ACRONYMS AND ABBREVIATIONS

<b>AI</b>	Artificial Intelligence
<b>aSAH</b>	Aneurysmal Subarachnoid Hemorrhage
<b>HUG</b>	Hospital Universitario de Getafe
<b>CNS</b>	Central Nervous System
<b>DCI</b>	Delayed Cerebral Ischemia
<b>TCD</b>	Transcranial Doppler
<b>CT</b>	Computed Tomography
<b>WFNS</b>	World Federation of Neurological Societies
<b>GSC</b>	Glasgow Coma Scale
<b>ROC AUC</b>	Receiver Operating Characteristic - Area Under the Curve
<b>IVH</b>	Intraventricular hemorrhage
<b>HU</b>	Hounsfield Units
<b>DICOM</b>	Digital Imaging and Communications in Medicine
<b>MLR</b>	Multiple Logistic Regression
<b>ANNs</b>	Artificial Neural Networks
<b>ML</b>	Machine Learning
<b>ICU</b>	Intensive Care Unit
<b>IoU</b>	Intersection over Union
<b>TP</b>	True Positives
<b>FP</b>	False Positives
<b>TN</b>	True Negatives
<b>FN</b>	False Negatives
<b>w</b>	Logistic regression weight
<b>AP</b>	Average Precision

**CEIm** Comité de Ética de la Investigación con medicamentos

**HCIS** Hospital Information System



# 1. INTRODUCTION

## 1.1. Aim and Motivation

In the field of medical science, artificial intelligence (AI) has shown potential in enhancing diagnostic accuracy, treatment planning, and patient outcomes [1]. By analyzing available clinical data, this technology is also useful in managing cases where outcomes are difficult to predict, such as in patients with subarachnoid hemorrhage.

Subarachnoid hemorrhage (SAH) is a critical neurological condition that requires early and precise intervention due to its high morbidity and mortality rates. It can lead to severe complications including cerebral vasospasm, which involves the narrowing of cerebral arteries, potentially resulting in unfavorable outcomes such as ischemia and stroke [2], [3]. Therefore, being able to predict vasospasm is crucial in reducing these risks and developing patient-specific therapeutic strategies. Although different grading scales have been proposed to predict vasospasm based on clinical or radiological factors, these scales often have low predictive value and high interobserver variability [4].

Recent advancements in AI, particularly in image segmentation, have provided new ways of improving the management of SAH patients. AI-based quantification and assessment of SAH severity scores can be used as predictive markers for the development of vasospasm [1]. Consequently, healthcare professionals can gain deeper insights into a patient's condition, enabling earlier intervention and personalized care plans [5].

This thesis aims to explore the efficacy of AI segmentation tools in assigning severity scores to SAH patients, reducing interobserver variability and ultimately predicting the onset of vasospasm in affected patients.

The project was conducted in collaboration with the Hospital Universitario de Getafe (HUG), a centre for which this study is particularly relevant. This hospital is a reference centre for the treatment of SAH in the South of Madrid, and the incidence of aneurysmal SAH (aSAH) has been increasing over time. In the last 11 years, 198 cases of aSAH have been treated at HUG, of which 13% suffered clinical vasospasm and 20% had a cerebral infarction; 17% of patients admitted for aSAH died.

## 1.2. Subarachnoid Hemorrhage and Cerebral Vasospasm

Subarachnoid hemorrhage (SAH) is the accumulation of blood in the subarachnoid space, which is the area between the arachnoid membrane and the pia mater surrounding the brain (Figure 1.1). SAH can lead to central nervous system (CNS) deficits and other serious complications, including vasospasm, delayed cerebral ischaemia (DCI), hydrocephalus, rebleeding and cerebral edema [6].

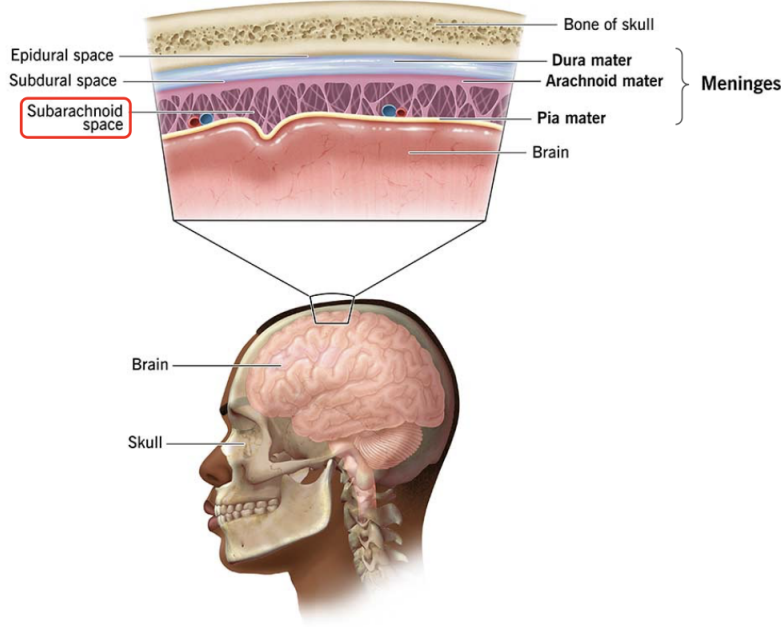


Fig. 1.1. Schematic view of the meninges. The meninges are a set of three membranes that provide protection and cover for the CNS, which includes the brain and spinal cord. There are three spaces within the meninges. The subarachnoid space is located between the arachnoid mater and pia mater, and is filled with cerebrospinal fluid which serves to cushion and protect the brain and spinal cord. Source: [7]

SAH can be caused by either non-traumatic factors (with about 85% resulting from aneurysm rupture) (Figure 1.2) or traumatic injury. Although aSAH represents only 5% of all strokes, it has the highest mortality and disability rates [8].

The three most common sites for aneurysm rupture are the junction of the posterior communicating artery and internal carotid artery (about 40%), the anterior communicating artery/anterior cerebral artery complex (about 30%), and the main branch of the middle cerebral artery (about 20%) [9]. The triggering factors for aneurysm rupture are complex. In some patients, rupture is thought to be caused by an unexpected increase in blood pressure. Activities preceding a aSAH, such as exercise and sexual activity, are reported in over 20% of cases [10].

The incidence of aSAH is approximately 10 cases per 100,000 per year. Approximately 11% of patients die before receiving medical attention and an additional 40% die within four weeks after being admitted to the hospital [12].

A recent study carried out by Xia *et al.* [13] has found significant variations in the annual incidence of aSAH based on sex, age, and ethnicity. Women had a higher incidence than men, and the incidence increased with age in both sexes. Among the different racial and ethnic groups studied, black patients had the highest incidence of aSAH, in contrast to non-Hispanic white patients and other groups. These findings highlight the significance of taking into account both demographic and ethnic factors when assessing the risk of

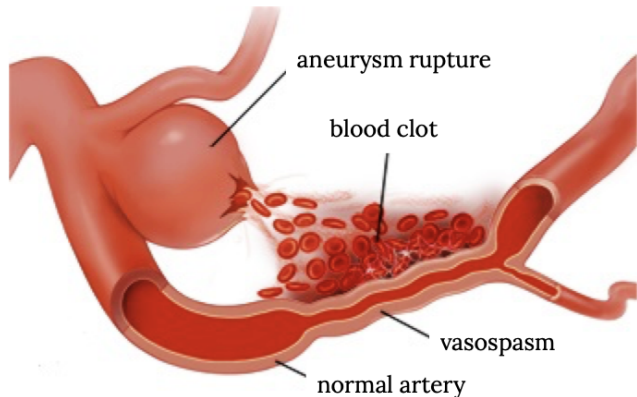


Fig. 1.2. Schematic illustration of an aneurysm. This diagram shows a ruptured aneurysm on a blood vessel, highlighting the release of blood into the surrounding area, which can lead to blood clot formation and vasospasm in adjacent vessels. Source:[11]

aSAH.

Despite advances in diagnosing and treating aSAH, available therapeutic options continue to be limited, resulting in unsatisfactory clinical outcomes [12]. In the literature, authors have used different methods to define vasospasm, including terms such as symptomatic or clinical vasospasm, transcranial Doppler vasospasm and angiographic vasospasm [14]. However, vasospasm remains poorly understood, predicted and ultimately treated [15].

Cerebral vasospasm is presented as a focal neurological deficit detected during physical examination, confirmed by the constriction of a cerebral blood vessel observed through computed tomography (CT) - angiography or conventional angiography (Figure 1.3).

Typically, the clinical syndrome resulting from cerebral vasospasm is DCI and is characterized by the onset of new focal neurological symptoms and/or loss of consciousness lasting over an hour in patients with aSAH [16], [17]. In patients with symptomatic cerebral vasospasm, up to 50% may progress to DCI. It is therefore important to identify those individuals who are at risk of developing vasospasm [18].

Transcranial Doppler (TCD) remains the only non-invasive vasospasm diagnostic modality in clinical use that consistently demonstrates high sensitivity and specificity. However, the delay between changes in TCD velocities and the onset of subsequent ischemia often prevents timely and effective early intervention in many patients. Moreover, since TCD velocity changes manifest after the blood vessels have already begun to narrow, treatments initiated at this point may be less effective [19].

The main current treatment for cerebral vasospasm includes oral nimodipine, which has shown to reduce the risk of ischemic complications. Nimodipine is a calcium channel blocker that dilates cerebral arteries. Additionally, aggressive management of cerebral perfusion through induced hypertension (elevation of blood pressure) is usually employed to increase blood flow to ischemic brain regions [20]. Overall, the timing of interventions

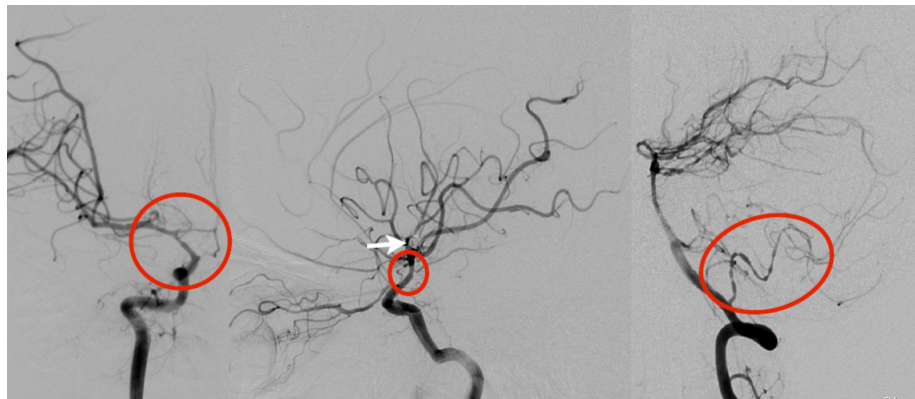


Fig. 1.3. Digital angiography study, highlighted by three red circles, showing evidence of angiographic cerebral vasospasm. The first image shows cerebral vasospasm at the terminal end of the carotid artery and at the beginning of the middle and anterior cerebral arteries. The second image shows cerebral vasospasm in the carotid siphon and the third image shows widespread and localised vasospasm in the posterior inferior cerebellar artery. The white arrow indicates an aneurysm occluded by internal platinum coils. Source: [22]

is crucial to effectively reduce the risk of DCI and other complications [21].

### 1.3. Clinical and Radiological Scores after aSAH

Currently, clinical decisions for aSAH patients are primarily guided by the assessment of grading systems that evaluate both clinical and radiological features.

Clinical scales include the Hunt and Hess scale, which classifies patients according to the severity of their post-SAH symptoms, ranging from mild headache (grade I) to deep coma (grade V) [23]. Another example is the World Federation of Neurosurgical Societies (WFNS) grading system, which is similar to the Hunt and Hess scale but includes modifications for motor response and replaces the original Glasgow Coma Scale (GCS) score component. It is used to assess the initial neurological status for therapeutic decision making [24]. However, none of these scales were originally designed to assess the prediction of vasospasm.

Two widely recognized radiological scoring systems to evaluate the likelihood of vasospasm are the Fisher Scale [25] and the Modified Fisher Scale [26], each serving as valuable tools based on initial brain imaging findings, typically CT scans (Table 1.1). Both scales are used to guide clinical decisions regarding the intensity of monitoring, preventive strategies, and therapeutic interventions for patients with aSAH. The scales assist in guiding these decisions by stratifying risk based on imaging rather than clinical symptoms alone, thereby allowing for the implementation of early and targeted interventions [27], [28].

Nevertheless, the predictive accuracy of Fisher's Scale has been called into question. When grades 3 and 4 are grouped into a single category to simplify the analysis of the

predictive value of vasospasm, the Fisher Scale presents a relatively modest area under the curve (AUC) value of 0.545, sensitivity of 84.6% and specificity of 36.6% (data from the HUG). In contrast, the Modified Fisher Scale, introduced in 2006, enriches its predictive capacity by integrating additional radiological parameters such as intraventricular hemorrhage (IVH), leading to a higher AUC value of 0.617, with sensitivity of 85.1% and specificity of 50.4% [29]. Consequently, while both scoring systems offer valuable insights into risk stratification for aSAH patients, exploring new methodologies that yield higher AUC values for vasospasm prediction would be relevant.

TABLE 1.1. MAIN CT SCALES FOR ASAHI EVALUATION.

Clinical Grade	Fisher, <i>et al.</i> [25]	Claassen, <i>et al.</i> (Modified Fisher) [26]
0	-	No SAH or intraventricular hemorrhage
I	No SAH visualized	Minimal or thin SAH without intraventricular hemorrhage; low risk of vasospasm
II	Diffuse or thin blood (vertical layers < 1 mm thick)	Minimal or thin SAH with intraventricular hemorrhage
III	Localized clot and/or vertical layers of blood (>1 mm thick)	Thick cisternal clot without intraventricular hemorrhage; intermediate risk of vasospasm
IV	Diffuse SAH or none, but with intraventricular or intraparenchymal clot	Thick cisternal clot with intraventricular hemorrhage; high risk of symptomatic vasospasm

#### 1.4. Head Computed Tomography

Computed Tomography (CT) scan combines X-ray technology with sophisticated computer processing to generate detailed images of internal body structures. In this procedure, a focused beam of X-rays is aimed at the patient and rapidly rotated around them. This ro-

tation enables the machine's computer to interpret the signals and generate cross-sectional "slices", or tomographic images, of the scanned area. These images provide physicians with more accurate information than conventional X-rays by showing bones, muscles, fat, organs and blood vessels in great detail. The individual slices can be digitally joined together to create a three-dimensional (3D) image, providing a comprehensive view that makes it easier to identify underlying structures, tumours or other abnormalities, thereby improving diagnostic accuracy [30], [31].

If aSAH is clinically suspected, the recommended initial diagnostic test is a non-contrast cranial CT scan (Figure 1.4). Under appropriate conditions, it is needed to obtain this scan with thin slices (3 mm) through the basal cisterns for detailed assessment [9]. On a CT scan, aSAH appears as a linear hyperdense lesion.

The diagnostic accuracy of a CT scan is typically around 90%. In the first 12 hours after an aSAH, sensitivity is 98-100%, dropping to 93% at 24 hours and 57-85% by the sixth day. The detection rate drops sharply as blood circulates in the subarachnoid space and the cerebrospinal fluid (CSF) clears. Typically, aSAH is almost completely cleared within 10-14 days [32], [33].

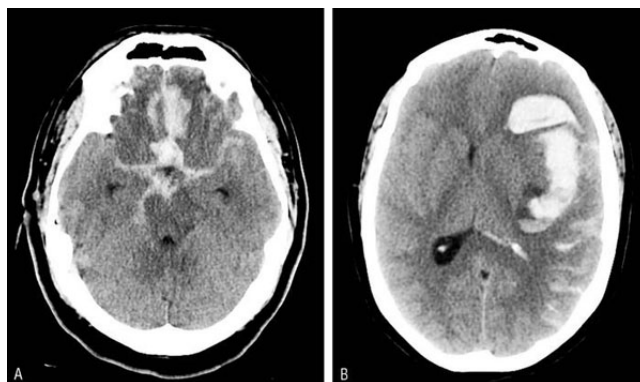


Fig. 1.4. CT images of patients with aSAH, Fisher grade IV. Case A shows a typical image of a ruptured aneurysm of the anterior communicating artery. Case B shows an image of SAH with intraparenchymal haematoma resulting from the rupture of a left middle cerebral artery aneurysm. Source: [34]

#### 1.4.1. Hounsfield Units

Hounsfield units (HU) serve as a dimensionless unit extensively used in CT scans to standardize and conveniently represent CT numbers [35]. HU are derived from a linear transformation of the measured attenuation coefficients:

$$HU = \left( \frac{\mu_{\text{material}} - \mu_{\text{water}}}{\mu_{\text{water}}} \right) \times 1000 \quad (1.1)$$

$\mu$  = CT linear attenuation coefficient

Where the arbitrarily-assigned radiodensities for air and pure water are as follows:

- The radiodensity of distilled water at Standard Temperature and Pressure (STP) — defined as a temperature of 0 °C and a pressure of 105 pascals (equivalent to sea-level conditions) — is 0 HU.
- The radiodensity of air at STP is -1000 HU.

Therefore, values ranges from -1000 HU for air to around 2000 HU for very dense bone [36]. In other words, denser tissues (such as cranial bone or blood in Figure 1.4) will appear whiter on the CT image because they have higher HU and absorb more X-rays. Conversely, air will appear black due to its very low HU, indicating it absorbs fewer X-rays. Less dense tissues, such as fat or certain soft tissues, will appear in varying shades of gray, darker than denser tissues but lighter than air, reflecting their intermediate HU values.

#### 1.4.2. DICOM images

The Digital Imaging and Communications in Medicine (DICOM) standard is a global standard that specifies a format for the storage of medical images and a protocol for facilitating data exchange among medical imaging systems [37].

DICOM standard is of great importance for the management of medical images and associated metadata. It ensures that every image file includes a comprehensive metadata scheme that provides detailed descriptions of the subject and procedures used to produce the image, which is of critical importance for medical use in clinical evaluations, management, and research. The metadata, together with the image data, is stored in a structured file comprising a preamble, prefix, header (which includes patient information and study parameters), and pixel data. These components are essential for maintaining the integrity and utility of the data, preventing any accidental separation of the image from its descriptive information [37], [38].

In its simplest form, the DICOM data model organizes the information of medical images into a structured hierarchy, as shown in Figure 1.5.

The CT images used in this project are in the DICOM format (.dcm).

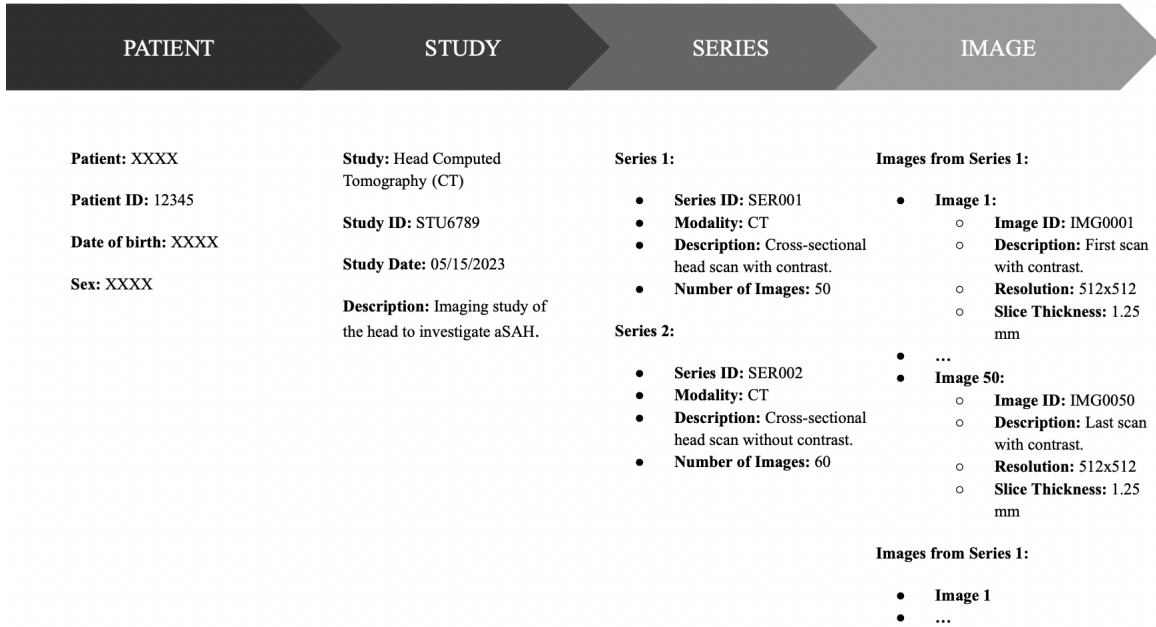


Fig. 1.5. Example of the DICOM hierarchical structure for organizing medical images, demonstrating the Patient-Study-Series-Image model with detailed information for each level.

## 1.5. Medical image segmentation

Image segmentation represents a crucial step in image analysis. Its purpose is to extract meaningful information from an image by segmenting it into regions or objects (Figure 1.7). This process facilitates object representation and feature measurement, allowing for a more detailed and accurate analysis of the image data [39].

Typically, physicians perform this process manually, slice by slice, which can be both time-consuming and laborious. Various computer-aided segmentation techniques (Figure 1.6) have been developed to address this issue, as discussed in the literature. These methods can generally be categorized into three types: automatic (unsupervised), interactive (semi-supervised), and supervised methods [40].

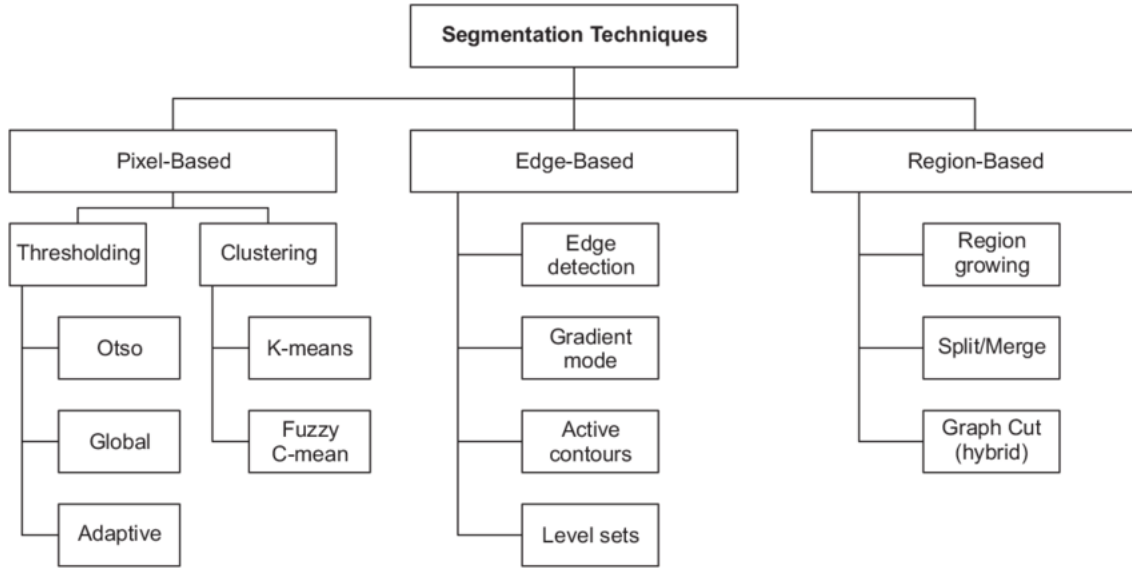


Fig. 1.6. Overview of Image Segmentation Techniques: Pixel-Based, Edge-Based, and Region-Based Approaches. Source: [41]

While supervised segmentation methods require the manual labelling of training data in order to identify specific objects within images, automatic approaches provide segmentation results without the necessity for prior knowledge of the images themselves and without the need for user interaction [40].

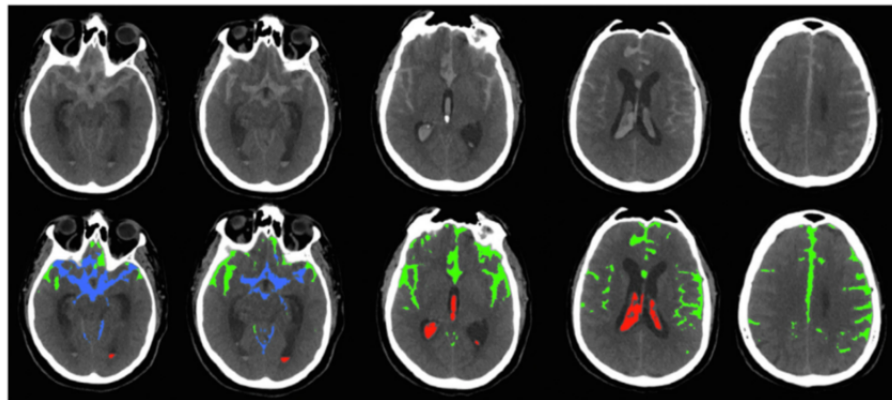


Fig. 1.7. Automated Blood Segmentation Results for a Subarachnoid Hemorrhage Patient's Admission CT Scan. Original axial brain CT images at five different levels (top row) juxtaposed with their corresponding segmentation results (bottom row). The segmented images highlight cisternal blood in blue, sulcal blood in green, and ventricular blood in red. Source: [42]

### 1.5.1. U-Net

A specific instance of the supervised segmentation technique that will be used in this project is the U-Net model, which was proposed by Ronneberger *et al.* during the MIC-

CAI 2015 conference [43]. U-Net is a convolutional neural network (CNN) type known for its effectiveness in biomedical image segmentation. Its distinctive "U"-shaped architecture, from which it derives its name, consists of a contracting path for context capture and a symmetric expanding path for precise localization (Figure 1.8), making it useful for tasks where both context and localization are important. Ronneberger *et al.* network's design eliminates the need for fully connected layers and instead relies on upsampling and feature concatenation to provide high-resolution output maps. U-Net is distinguished by its ability to function effectively with a limited number of training images, following extensive data augmentation techniques to enhance performance and facilitate generalization from limited data [43].

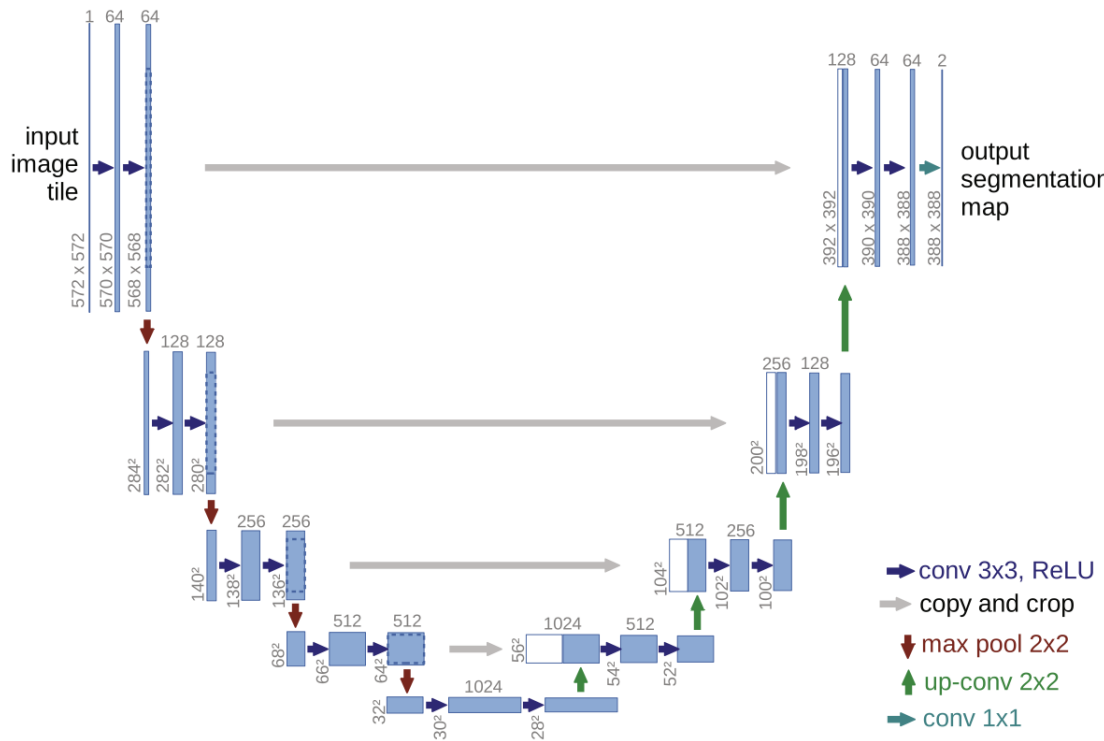


Fig. 1.8. U-net architecture exemplified for 32x32 pixels at the lowest resolution. Each blue box represents a multi-channel feature map, with the number of channels indicated at the top. The x-y dimensions are provided at the bottom left corner of each box. White boxes indicate duplicated feature maps. The arrows delineate various operations within the architecture. Source: [43]

## 1.6. Objectives

### 1.6.1. Primary Objective

The primary objective of this project is to evaluate the precision of AI-based segmentation tools in assigning the modified Fisher Score (a method for quantifying aSAH from initial basal CT scans to predict vasospasm) in aSAH patients. The ultimate goal is to em-

ploy this technology in order to predict the onset of vasospasm in those affected, thereby allowing for more effective management of the condition.

### 1.6.2. Secondary Objectives

To support the primary objective, the project will focus on a number of key goals:

1. **Model Development:** Develop a machine learning (ML) model to perform image segmentation and accurately measure volume, density, thickness and localization of aSAH.
2. **Automated Scale:** Train a ML model to automatically assign the modified Fisher Scale.
3. **Variability Assessment:** Evaluate the variability in manual measurements of the modified Fisher Score assigned by two different neuroradiologists to establish a baseline for comparison, using Kappa coefficients. The modified Fisher assigned by the neuroradiologists served as the gold standard for the automated scale model.
4. **Predictive Evaluation:** Compare the modified Fisher Score obtained manually and automatically to assess their predictive capability for the development of vasospasm.
5. **Extended Evaluation:** Analyze the predictive power of an "extended modified Fisher Scale", incorporating additional variables (hemorrhage volume, thickness and patient's age) alongside the modified Fisher Score, to enhance vasospasm prediction.

In conclusion, the core purpose of this study is to transform the prediction and management of vasospasm in patients with aSAH through the application of AI-driven segmentation techniques and comprehensive predictive modeling. To accomplish this, a first model was developed to automatically assign the modified Fisher Scale. Then, by suggesting the AI-proposed grade to the physician, the interobserver variability will be reduced, enhancing the predictive value of the modified Fisher Scale. Finally, different segmentation features will be added to the modified Fisher Scale to create a classifier for vasospasm prediction.

### 1.7. Project Timeline

Figure 1.9 represents the Gantt diagram corresponding to the present thesis, illustrating the timeline for the different stages of the project.



Fig. 1.9. Gantt Diagram: Comprehensive timeline and milestones for this thesis development.  
(Seg.: Segmentation)

## 2. STATE OF THE ART

### 2.1. Systematic review

From September 2023 to December 2023, my colleague Sofía Carlota Lucena Núñez and I conducted a systematic review during our internship at the HUG, under the supervision of Dr. José Ángel Lorente Balanza. Our objective was to gain a comprehensive understanding of the current scales used in clinical practice for predicting vasospasm and their accuracy values, as well as to prove the relevance of the present thesis. Our findings indicated that there is considerable scope for improvement, particularly in relation to the most commonly used scale, the Fisher scale, which exhibited an AUC of only 0.545. Consequently, we proceeded to expand our research to encompass risk assessment systems that incorporate AI techniques.

Despite decades of intensive research, a conclusive treatment for cerebral vasospasm subsequent to aSAH remains elusive. Thus, accurately predicting vasospasm becomes pivotal in improving decision-making in diagnostic imaging, patient triage, and prognosis. The ability to identify individuals prone to developing cerebral vasospasm would signify a notable advancement in managing patients with aSAH [44].

#### 2.1.1. No AI-Based Risk Scales

In addition to the most commonly used scale proposed by Fisher *et al.* in 1980 [25], a prior radiographic grading scale was proposed in 1978 by the Japanese researchers Takemae *et al.* [45], [44]. In 1990 Hijdra *et al.* [46] presented another scale based solely on the CT image, where the amount of blood in ten basal cisterns and in four ventricles was graded separately, resulting in an AUC of 0.678 for the prediction of DCI [47].

Additionally, other authors have developed novel grading scales that integrate both radiological and clinical scores. Oliveira Souza *et al.* [48] proposed VASOGRADE, a combination of the modified Fisher scale [26] and the WFNS grading system [24] for the stratification of DCI after aSAH, with an AUC of 0.67.

The following risk factors have been identified as associated with cerebral vasospasm: clot thickness, volume and density; rate of clearance; presence of IVH; cocaine use and smoking [44], [49], [25], [26], [19], [50], [51].

Furthermore, Quereshi *et al.* [52] employed stepwise logistic regression analysis to identify predictors of symptomatic vasospasm from demographic, clinical and radiological characteristics among 283 patients. Finally, they developed a scoring system, known as the Symptomatic Vasospasm Index, which combined four independent predictors: the thickness of the aSAH clot, an early increase in middle cerebral artery mean flow velocity

on or before day 5, a GCS score less than 14, and the rupture of an anterior cerebral or internal carotid artery aneurysm. This scoring system performed better than when using the predictors separately [44].

Multiple logistic regression (MLR) models forecast outcomes by estimating linear relationships among input variables, which may pose a significant limitation. Conversely, an artificial neural network (ANN) -based model can overcome this constraint by accounting for complex nonlinear relationships among the variables. [44].

### 2.1.2. AI-Based Risk Scales

AI has brought innovative changes in numerous fields, including medical science. AI is able to substantially improve diagnostic accuracy, treatment planning, and patient outcomes [53].

Previous studies have attempted to predict vasospasm following aSAH with ANNs. ANNs are a form of AI that simulate intelligent behavior by mimicking the functioning of biologically generated neural networks [54]. Dumont *et al.* [55] provide an example of this, designing a simple ANN based on clinical and radiographic factors and testing its predictive ability against existing MLR models. The ANN demonstrated a superior predictive capacity compared to the MLR models, with an AUC of 0.960. Furthermore, Skoch *et al.* [54] attempted to create another ANNs with demographics, clinical, radiological, and outcome data for the prediction of vasospasm in the paediatric population (aged <21 years), concluding that adult-derived aSAH value nodes can be effectively applied to an ANNs model to accurately predict symptomatic vasospasm in children.

Other approaches include ML models, as exemplified by the work of Savarraj *et al.* [56]. The ML model was trained to predict DCI and other functional outcomes using data collected within three days of admission, with an AUC of 0.75. Similarly, Ramos *et al.* [57] conducted three distinct analyses to predict DCI. The first was a logistic regression model, which assessed the prognostic value of known predictors (AUC of 0.63). The second was an ML model created using all clinical variables (AUC of 0.68). The third was an ML model created by combining clinical data with image features extracted from CT images using an autoencoder (AUC of 0.74).

Nevertheless, AI models that have demonstrated the highest predictive accuracy include those that incorporate cranial CT image features. However, in most cases, data was collected by a radiologist serving as input variables for ANNs, rather than being directly examined by the model. CT image analysis and segmentation models have been used to address other issues closely related to prediction of vasospasm. Thanellas *et al.* [58] segmented hemorrhage in non contrast CT images with a U-Net based model to identify and localize aSAH with a sensitivity of 99.3% and specificity of 63.2%.

An interesting approach, which involves the application of quantitative radiographic image markers to predict clinical complications following aSAH, was proposed by Danala

*et al.* [59]. The pilot study comprised a fully-automated computer-aided detection (CAD) scheme, which was applied to segment intracranial brain regions into four subregions: CSF, white matter (WM), grey matter (GM), and leaked extra - parenchymal blood (EPB). The CAD system then identified the sulci and computed nine image features related to five segmented volumes: sulci, EPB, CSF, WM, and GM. Additionally, it calculated four volumetric ratios relative to the sulci. Finally, sixteen support vector machine (SVM) models were developed using CT images from either the time of admission or prior to discharge. The objective was to predict eight clinically relevant parameters for assessing patient prognosis. The AUC for the SVMs ranged from 0.62 to 0.86.

In addition to the models presented in this section, there are few examples of AI models used for aSAH prognosis. However, no studies were found that used AI techniques for the assignment of existing vasospasm risk scales.

In conclusion, while several risk scales exist to predict unfavorable outcomes of aSAH, there is an urgent need to develop an accurate scale specifically for predicting vasospasm. Hence, this project holds particular significance not only for its capacity to accurately segment aSAH, measure hemorrhage features and assign the modified Fisher Scale, but also for its potential in ultimately predicting vasospasm. Moreover, being able to predict vasospasm could fundamentally change the management of these patients, leading to improved outcomes.

### **3. MATERIALS AND METHODS**

Prior to outlining the methodology, it is essential to consider certain operative definitions for the purpose of this bachelor thesis. These are as follows:

1. **Aneurysmal Subarachnoid Hemorrhage (aSAH):** accumulation of blood in the subarachnoid space resulting from an aneurysm rupture. At the HUG setting, the SAH diagnosis entails an initial evaluation by on-call radiologists based on non-contrast CT scans, subsequently validated by a neuroradiologist. The confirmation of an aneurysm rupture is achieved through angioCT or arteriography.
2. **Vasospasm:** constriction of a cerebral blood vessel observed through TCD, CT-angiography or conventional angiography, where:
  - Clinical Vasospasm: vessel constriction manifests as clinical symptoms, such as focal neurological deficits or a decrease of 2 or more points on the GCS.
  - TCD Vasospasm: vasospasm is confirmed by TCD ultrasound.
  - Arteriographic Vasospasm: vasospasm is confirmed by arteriography.
3. **Mortality:** death within the Intensive Care Unit (ICU) at HUG.

#### **3.1. Study Design and Methodology**

The project is a retrospective cohort observational study. It will examine cases of aSAH admitted to the ICU of the HUG from 2012 to 2023, totalling 198 cases. Only those cases that meet all the inclusion criteria and none of the predefined exclusion criteria will be included in the study.

The inclusion criteria are as follows:

1. Patients admitted to the ICU from November 15, 2012, to October 1, 2023 (the period during which aSAH cases were collected in the ICU).
2. Admission diagnosis of aSAH confirmed by non-contrast CT scan.

The exclusion criteria are as follows:

1. Patients who died within the first three days of ICU admission.
2. Transfer from another hospital with more than 48 hours since the diagnosis of aSAH.

3. Absence of available imaging tests for analysis.
4. Presence of changes in the CT scan prior to the current episode (e.g., previous hemorrhages or cerebral infarctions, tumors) that hinder the identification of anatomical changes specifically due to the current episode of aSAH.
5. Age under 16 years.

In order to achieve the primary objective of automatically assigning the modified Fisher scale, a U-Net model was initially trained to segment the CT images. This allowed for the calculation of the hemorrhage's volume, thickness, density, and location. Additionally, other image features were manually collected and modified Fisher labels were assigned to the images by two different neuroradiologists individually. Therefore, inter-observer variability measurement was possible. Subsequently, multiple classifier models were developed to assign the modified Fisher scale. This enabled a comparison of results and the importance of each variable. Moreover, the ability of the manual and AI scales to predict vasospasm was quantified. Finally, a straightforward classification model was developed to predict vasospasm directly, using the calculated modified Fisher scale, and hemorrhage's volume, thickness and patient's age.

### **3.2. Patient Population and Data Collection**

As previously mentioned, 198 cases of aSAH were collected between 2012 and 2023. In the ICU database, baseline characteristics (i.e., age and sex), severity scales (i.e., Hunt and Hess, GCS and Fisher), treatment options (i.e., nimodipine) and complications (i.e., vasospasm, cerebral infarction, rebleeding, epileptic seizures, hydrocephalus and mortality) are stored.

Data collection for this study involved obtaining CT images from the Radiology Department of the HUG, provided by the head of the department, Dr. Jorge Mario Sánchez. All images were in DICOM format. For each subject, the images were organized into separate folders corresponding to different series of non-contrast CT, contrast-enhanced CT, angiography and other extra folders with different pre-processing steps. It is important to note that the acquisition process was not consistent between patients, with some having more than 300 slices per CT scan and others having less than 40 slices. This variability in the number of slices per CT scan posed a challenge for consistent analysis and comparison of imaging data.

Subjects were pseudonymized (i.e., identifying information was replaced with artificial identifiers to protect the privacy of individuals' data) and identified as HSA 1, HSA 2, HSA 3, etc. In addition, the corresponding anonymized ICU database was provided for each patient, including demographic variables, clinical scales and other outcomes.

Figure 3.1 shows an example of how 2D slices are stored for the non-contrast series.

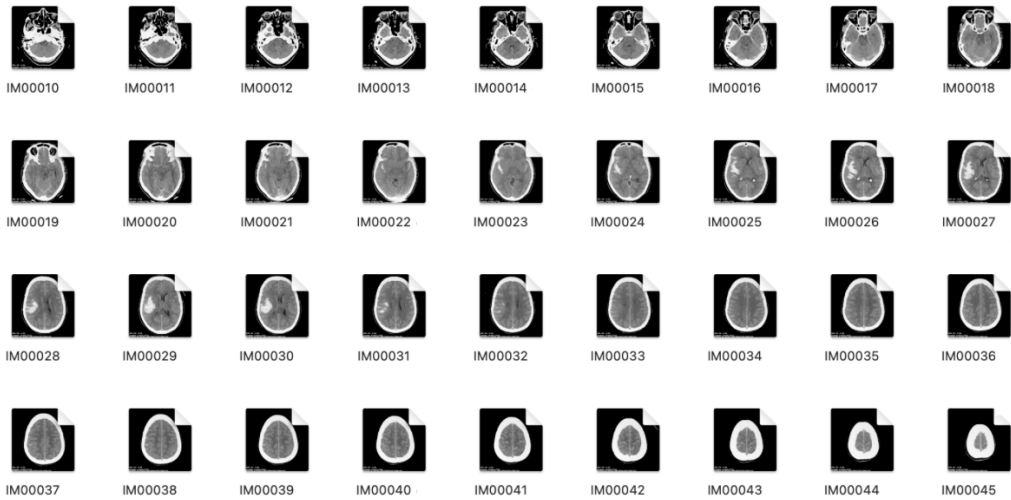


Fig. 3.1. Example of 2D slices from subject HSA 129, study ST00001, series SE00002.

It is important to note that basal and upper slices often contain more cranial bone, which can interfere with the segmentation process. Since each subject has a different number of slices in the acquisition, a single number of slices for removal could not be used for all cases. Therefore, to address this challenge different percentages for removal were tried. The initial interval for basal slices was [20%, 40%] and for upper slices was [10%, 20%]. By manually analyzing various options inside each interval, finally 35% of the initial slices and 20% of the final slices were arbitrarily removed. Although anatomical structures can vary between subjects, these percentages allowed us to retain the maximum number of valuable slices while removing the interfering ones effectively.

Furthermore, an extra database was created to include each subject's series of interest (non-contrast CT series with the maximum number of slices) and the presence of bleed, IVH and suprasellar cistern bleed, all in binary format.

### 3.2.1. Modified Fisher Scale Assessment by Neuroradiologists

The CT images from the subjects included in the study were labelled with the modified Fisher grade by two independent neuroradiologists from the Radiology Department at the HUG, with clinical comments included in those cases where necessary. This approach allows for the measurement of variability between physicians, as well as variability with respect to the proposed AI model measured using Cohen's Kappa coefficient.

### 3.3. Tools and Programming Environments Used

The main programming language used is Python, chosen for its versatility, extensive libraries and ease of use [60]. The Python code was developed using the Spyder Integrated Development Environment (IDE), which is part of the Anaconda distribution [61].

Furthermore, certain aspects of the project were conducted using 3D Slicer, a free and open-source software platform for biomedical image informatics, image processing, and three-dimensional visualization [62].

### 3.4. Segmentation

In relation with Objective 1 (Model Development) from the secondary objectives (see 1.6.2.), several approaches to hemorrhage segmentation have been proposed and compared to identify the best performing method. First, a basic thresholding-based segmentation approach was developed. Additionally, two different automated segmentation models were adapted for hemorrhage segmentation. Lastly, two final approaches were developed using either advanced or simple techniques within the 3D Slicer interface.

#### 3.4.1. Thresholding-based Segmentation

Threshold-based segmentation compares all pixels in a grayscale image to specified threshold values. Each pixel is then assigned to different categories based on whether its intensity is above or below these thresholds. This technique effectively separates different regions within the image by grouping pixels with similar intensity levels [63].

It is also possible to apply this technique to CT images. In these images, denser tissue is whiter (see 1.4.1.), so the hemorrhage can be segmented by simply thresholding the histogram. A histogram visually represents the frequency of pixel intensities in an image, indicating how many pixels correspond to each intensity value [64], [36].

The thresholded image is therefore defined as:

$$g(x, y) = \begin{cases} 1 & \text{if } f(x, y) > T \\ 0 & \text{if } f(x, y) \leq T \end{cases} \quad (3.1)$$

where:

- $f(x, y)$  is the original image intensity at the pixel  $(x, y)$ .
- $g(x, y)$  is the thresholded image at the pixel  $(x, y)$ .
- $T$  is the threshold value.

This concept was translated into the Python programming language.

Firstly, as preprocessing, the DICOM image metadata attributes of '*RescaleIntercept*' and '*RescaleSlope*' were retrieved and used to convert the raw pixel values into calibrated intensity values by the following equation:

$$\text{Image} = \text{Image} \times \text{RescaleSlope} + \text{RescaleIntercept} \quad (3.2)$$

Furthermore, values for window level and window width (used to enhance contrast on specific intensities when visualizing on a screen, without modifying the original values) were extracted from the DICOM metadata and applied to the transformation.

Finally, a basic manual thresholding process based on the histogram was employed in order to obtain the segmented image.

### 3.4.2. Automated Segmentation Models

#### Pre-trained MONAI Tumor Segmentation Model

Project MONAI is an open-source, freely available collaborative framework designed to facilitate research and clinical collaboration in medical imaging [65]. Additionally, the MONAI Model Zoo is a repository of pre-trained models specifically designed for medical imaging tasks. It provides a variety of deep learning models that can be readily used or fine-tuned for different applications, including classification, segmentation, and anomaly detection.

A tumor segmentation model was employed from this Model Zoo. This was a pre-trained model for volumetric (3D) segmentation of brain tumour subregions from multi-modal magnetic resonance imaging (MRI) based on BraTS (Brain Tumor Segmentation) challenge database [66]. The model consists on a network called SegResNet, which is similar to U-Net, and is designed and trained with the specific task of segmenting three distinct nested subregions of primary brain tumors, specifically gliomas. These subregions are identified as the "enhancing tumor" (ET), the "tumor core" (TC), and the "whole tumor" (WT). To accomplish this segmentation task, the model uses information from four MRI scans that are aligned: T1c, T1, T2, and FLAIR (Figure 3.2).

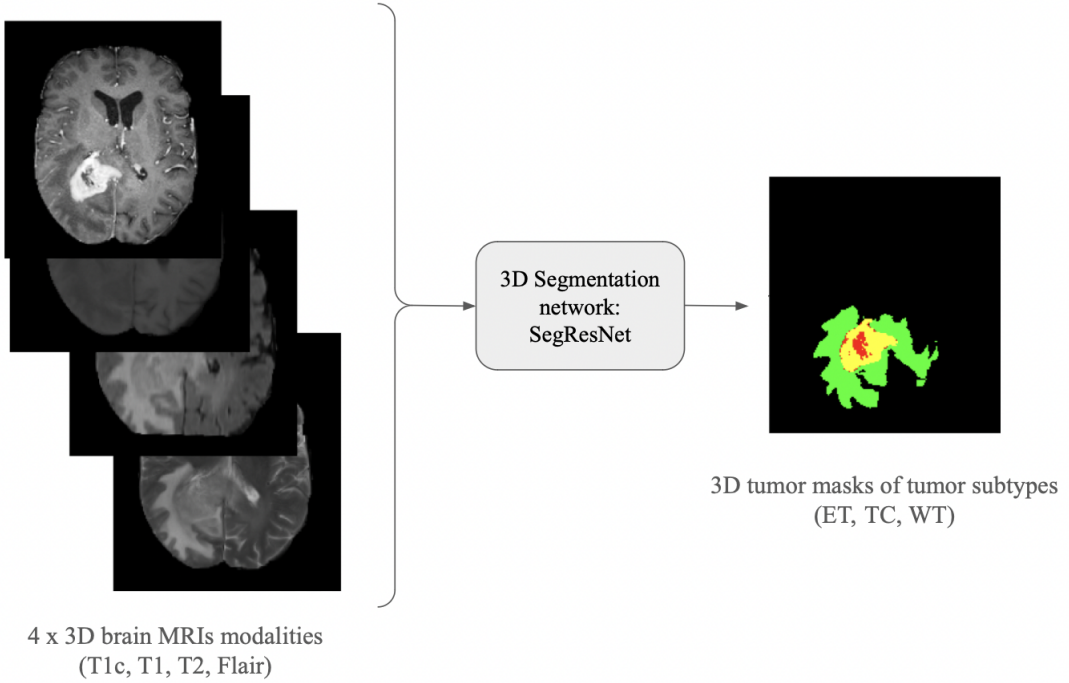


Fig. 3.2. Workflow for 3D segmentation of brain tumor subtypes by MONAI Model. Four modalities of brain MRI scans (T1c, T1, T2, Flair) are used as input for the 3D Segmentation network SegResNet, which outputs masks of tumor subtypes (ET, TC, WT). Source: [66]

Consequently, the model was designed to accept input images with four initial channels (T1c, T1, T2, Flair), whereas aSAH CT images only present one channel. To address this discrepancy, several modifications were implemented in the code to enhance preprocessing, data format compatibility, and ultimately, segmentation. Preprocessing approach included replicating the image in four channels, ensuring the expected input format and that no details were lost, and a simple window level and width adjustment.

The results were analyzed using the Dice Similarity Coefficient, a statistical measure that ranges from 0 to 1. This is employed to evaluate the similarity between two sets. In the context of image segmentation, it compares the overlap between the predicted segmentation and the ground truth:

$$\text{Dice} = \frac{2|A \cap B|}{|A| + |B|} \quad (3.3)$$

Where A and B are the sets of predicted and ground truth pixels, respectively.

### **U-Net Segmentation Model**

Secondly, a brain CT segmentation model based on a U-Net architecture (see 1.5.1.) by Sakib *et al.* [67] was consulted and trained for cerebral hemorrhage segmentation.

The training and validation of the model were conducted using a dataset sourced from

a public Kaggle database. This dataset consisted of 100 normal CT images and 100 hemorrhagic CT images in .png format of size (256, 256) pixels, which were labelled and catalogued in a CSV file collected via Google [68]. To enhance the dataset's variability, unique data augmentation techniques, including non-linear transformations like Twirl and Spherical, were employed alongside traditional data augmentation methods.

1. *Twirl Transformation*: rotates the hemorrhagic region around a central point, typically the center of the hemorrhage  $(x_c, y_c)$ . For multiple hemorrhagic areas, the centroid is calculated to apply the rotation. For transformed coordinates  $(x, y)$ :

$$x = \begin{cases} x_c + r \cdot \cos(\beta), & \text{for } r \leq r_{max} \\ x', & \text{for } r > r_{max} \end{cases} \quad (3.4)$$

$$y = \begin{cases} y_c + r \cdot \sin(\beta), & \text{for } r \leq r_{max} \\ y', & \text{for } r > r_{max} \end{cases} \quad (3.5)$$

Displacement from center:

$$d_x = x' - x_c \quad (3.6)$$

$$d_y = y' - y_c \quad (3.7)$$

Radial distance:

$$r = \sqrt{d_x^2 + d_y^2} \quad (3.8)$$

Rotation angle:

$$\beta = \arctan(d_y, d_x) + \alpha \left( \frac{r_{max} - r}{r_{max}} \right) \quad (3.9)$$

Where:

- $(x, y)$ : Transformed coordinates.
- $(x', y')$ : Original coordinates.
- $(x_c, y_c)$ : Hemorrhage center coordinates.
- $\beta$ : Rotation angle.
- $r$ : Radial distance from the hemorrhage center.
- $r_{max}$ : Maximum radial distance for transformation.
- $\alpha$ : Maximum rotation angle at  $r = 0$  [40, 50, 60, 70 and 80 degrees].

Therefore, points within  $r_{max}$  are rotated according to the transformation equations, with rotation decreasing linearly with distance  $r$ , while points beyond  $r_{max}$  remain unchanged.

2. *Spherical Transformation*: rotates the hemorrhagic area around the center  $(x_c, y_c)$  of the hemorrhage, and this rotation is applied within the maximum radius ( $r_{max}$ ). The transformation creates a zoomed-in effect at the center, resembling a lens, with the deformation decreasing towards the periphery. For transformed coordinates  $(x, y)$ :

$$x = x' - \begin{cases} z \cdot \tan(\beta_x), & \text{for } r \leq r_{max} \\ 0, & \text{for } r > r_{max} \end{cases} \quad (3.10)$$

$$y = y' - \begin{cases} z \cdot \tan(\beta_y), & \text{for } r \leq r_{max} \\ 0, & \text{for } r > r_{max} \end{cases} \quad (3.11)$$

Where:

$$z = \sqrt{d_{max}^2 + d^2} \quad (3.12)$$

$$\beta_x = \left(1 - \frac{1}{\rho}\right) \cdot \sin^{-1} \left( \frac{d_x}{\sqrt{d_x^2 + z^2}} \right) \quad (3.13)$$

$$\beta_y = \left(1 - \frac{1}{\rho}\right) \cdot \sin^{-1} \left( \frac{d_y}{\sqrt{d_y^2 + z^2}} \right) \quad (3.14)$$

Where:

- $(x, y)$ : Transformed coordinates.
- $(x', y')$ : Original coordinates.
- $(x_c, y_c)$ : Center coordinates of the hemorrhage.
- $r$ : Radial distance from the center of the hemorrhage.
- $r_{max}$ : Maximum radial distance for transformation.
- $d_x = x' - x_c$
- $d_y = y' - y_c$
- $d = \sqrt{d_x^2 + d_y^2}$
- $\rho$ : Reflection index [1.12, 1.14, 1.16, 1.18 and 1.20].

In order to evaluate the performance of the model, the Dice coefficient and the Intersection over Union (IoU) were computed. The IoU is similar to the Dice coefficient, measuring the area of overlap between the predicted segment and the ground truth.

$$\text{IoU} = \frac{\text{Area of Overlap}}{\text{Area of Union}} \quad (3.15)$$

Where:

- Area of Overlap is the area where the predicted and ground truth areas intersect.
- Area of Union is the total area covered by both the predicted and ground truth areas combined.

### 3.4.3. 3D Slicer Segmentation

3D Slicer is a free and open-source platform designed for visualizing, processing, segmenting, registering, and analyzing medical, biomedical, and various other 3D images and meshes [62]. The segmentation module yielded two distinct approaches:

1. **Grow from seeds:** This technique follows a region growing segmentation, which identifies and clusters pixels or regions based on criteria of similarity. It begins with an initial seed pixel or region defined manually and progressively expands this seed by including adjacent pixels or regions that satisfy certain predefined conditions of similarity. This method ensures cohesive grouping of similar areas within an image [69].
2. **Total Segmentator Extension:** This extension incorporates an AI model known as "TotalSegmentator," which is engineered for fully automatic whole-body CT segmentation, leveraging a network architecture developed from nnU-Net [70]. nnU-Net represents an advanced evolution of the U-Net framework, providing enhanced capabilities for biomedical image segmentation [71]. The Total Segmentator allows users to choose specific segmentation tasks, including the cerebral bleed task featured in this section.

## 3.5. Segment Statistics

To complete Objective 1 (Model Development) (see 1.6.2.), once the segmentation model was created, the hemorrhage features that were useful for determining the modified Fisher scale and predicting vasospasm were computed.

### 3.5.1. Volume of the Segment

A program was developed to compute an approximate volume in milliliters (*ml*) by stacking all 2D slices from the same non-contrast series to form a 3D volume.

The program calculates the volume of the hemorrhage by first extracting the slice thickness and pixel spacing from the DICOM metadata. It then computes the voxel volume by multiplying the slice thickness with the pixel spacing values. The total number of segmented pixels is calculated by summing all the pixels identified as part of the hemorrhage in the volume data. This total pixel count is then multiplied by the volume of a single voxel to obtain the hemorrhage volume in  $mm^3$ . This process is repeated in a loop for each subject's volume.

Some subjects had the non-contrast series divided into two separate folders in the dataset. This issue was resolved using a conditional loop.

Volume data was stored automatically for each case in a .xlsx file.

### **3.5.2. Maximum Clot Thickness**

Computing the maximum clot thickness of the hemorrhage is very useful for comparing the extent of the hemorrhage.

This part of the code tracks the thickness of the segmented regions by incrementing a counter for consecutive slices with segmented pixels. If a slice has no segmented pixels, it compares the current thickness to the maximum recorded thickness and updates the maximum if necessary. Finally, it ensures the maximum thickness is updated after the last slice is processed.

Maximum thickness data was stored automatically for each case in a .xlsx file.

### **3.5.3. Hemorrhage Density**

This section computes the average density of the hemorrhage segment by analyzing the pixel intensities in HU (see 1.4.1.).

To compute the average density the function extracts the pixel values from the original image where the segmented image mask is equal to 1, representing the hemorrhage. If no hemorrhage pixels are found, the function returns a density of 0. If there are hemorrhage pixels, the function calculates the average HU value of these pixels. During the processing loop, whenever the mask indicates the presence of hemorrhage, the function computes the density for that slice and adds it to a cumulative density sum, while incrementing a counter for each slice with detected hemorrhage. Finally, the average density for the subject is calculated by dividing the cumulative density sum by the counter, ensuring the average density is set to 0 if no hemorrhage is detected.

Average density data was stored automatically for each case in a .xlsx file.

### **3.5.4. Hemorrhage Localization**

Finally, the program calculates the percentage of hemorrhage present in different sections of the CT image by dividing the image into a grid (Figure 3.3). Initially, a grid of size 5x5 is created to store the hemorrhage percentages. This is followed by an iteration over each section of the grid, during which the start and end rows and columns for each section are determined based on the overall dimensions of the reference image. For each section, the corresponding part of the segmented volume is extracted. The number of pixels within the section is then summed to identify the number of pixels representing hemorrhage. This number is then divided by the total number of segmented pixels and multiplied by 100 to calculate the percentage of hemorrhage in the section. If there are no segmented pixels (no hemorrhage), the percentage is set to 0.

Percentage of hemorrhage in each section was stored automatically for each case in a .xlsx file.

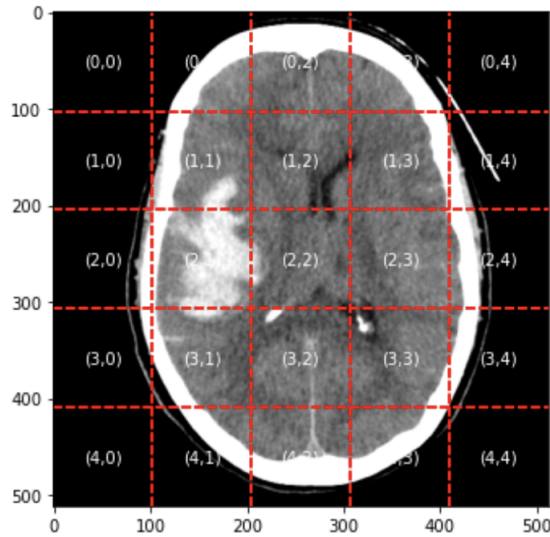


Fig. 3.3. Example from subject HSA 129 of original CT scan slice divided into a 5x5 grid. Each cell is labeled with its coordinates, allowing for detailed analysis of hemorrhage distribution across different sections of the brain.

Additionally, the presence of hemorrhage in column 2 was recorded as a key variable to determine the likelihood of hemorrhage in the central ventricles, that will be further used in the classifier for better localization interpretation and thus, better classification performance.

### 3.6. Modified Fisher Scale Classifier

To assess Objective 2 (Automated Scale) (see 1.6.2.), two different classification models were explored: Logistic Regression and Random Forest. Both models received the following inputs: ‘Patient’, ‘IVH’, ‘Bleed’, ‘Suprasellar cistern bleed’, each grid section with their corresponding percentages of total hemorrhage, ‘Hemorrhage in Column 2’, ‘MaxSliceThickness’, ‘AverageDensityHU’, and the modified Fisher scale assigned by a neuroradiologist. The last variable serves as the gold standard for the models.

Given the limited number of data samples (i.e., 143 scans), two different approaches were considered (see Table 1.1):

1. Binary model: Combines grades 0, 1, 2, and 3 together and treats grade 4 separately. This approach allows the model to distinguish subjects with the highest grade, indicating the highest risk.
2. Group the grades into broader categories:
  - Class 0: Combines grades 0 and 1
  - Class 1: Combines grades 2 and 3

- Class 2: Grade 4

This method is significant in clinical practice as it separates the highest grade 4 cases (with a vasospasm risk of 40%) from the medium grades. It is important to note that grades 2 and 3 have the same risk of vasospasm (around 33%). Grade 1 has a vasospasm risk of 24%, but due to the low number of cases in these grades, it is combined with grade 0.

### **3.6.1. Random Forest Classifier**

Following the preparation of the data, the program differentiates the data frame, the features (X), and the target labels (Y). The target labels are categorized based on the column with the modified Fisher scale assigned by the neuroradiologist, which is also removed from the feature set. Stratified K-Fold cross-validation with 10 splits is set up to ensure balanced class distribution. For each fold, the training data is oversampled using ADASYN to address class imbalance, followed by standardization. Hyperparameters for the Random Forest are optimized using GridSearchCV.

The model's predictions are evaluated using classification reports, ROC AUC, and precision-recall AUC metrics. These metrics are averaged and their standard deviations are calculated across folds. Furthermore, feature importance analysis is also conducted to illustrate how each feature is contributing to the model performance.

Confusion matrices are also used to evaluate the model's classification ability. A confusion matrix is a table in which true positives (TP) are the number of instances correctly predicted as positive; false positives (FP) are the number of instances incorrectly predicted as positive; true negatives (TN) are the number of instances correctly predicted as negative and false negatives (FN) are the number of instances incorrectly predicted as negative by the model (Table 3.1).

TABLE 3.1. CONFUSION MATRIX

	<b>Predicted Positive</b>	<b>Predicted Negative</b>
<b>Actual Positive</b>	TP	FN
<b>Actual Negative</b>	FP	TN

### **3.6.2. Logistic Regression Classifier**

Once more, the function that prepares data returns a data frame, features (X), and target labels (Y). Unnecessary columns are removed from the feature set. Stratified K-Fold cross-validation with 10 splits ensures balanced class distribution during training. For each fold, the training data undergoes oversampling using SMOTE to handle class imbal-

ance, followed by standardization. Hyperparameters for the Logistic Regression model are optimized using GridSearchCV.

The model's predictions are also evaluated using confusion matrices, classification reports, ROC AUC, and precision-recall AUC metrics. Additionally, the logistic regression weights are stored to understand each feature importance within the model.

### 3.7. Interobserver Variability and Model Comparison

Objective 3 (Variability Assessment) and Objective 4 (Predictive Evaluation) are examined in this section (see 1.6.2.). Variability between the modified Fisher scale proposed by two different neuroradiologists and the automated Fisher scale by both classifiers was measured using Cohen's Kappa coefficient. Kappa coefficient ranges from -1 to 1, being common categories:

- < 0: Poor
- 0 - 0.20: Slight
- 0.21 - 0.40: Fair
- 0.41 - 0.60: Moderate
- 0.61 - 0.80: Substantial
- 0.81 - 1.00: Almost perfect

Furthermore, both sensitivity and specificity in predicting vasospasm are computed for each bounded class as follows:

For Class 2 (grade 4) and Class 0 (grades 0 and 1):

- True Positives (TP): Class = 2 and vasospasm is 1
- False Positives (FP): Class = 2 and vasospasm is 0
- True Negatives (TN): Class = 0 and vasospasm is 0
- False Negatives (FN): Class = 0 and vasospasm is 1

For Class 1 (grades 2 and 3) and Class 0 (grades 0 and 1):

- TP: Class = 1 and vasospasm is 1
- FP: Class = 1 and vasospasm is 0
- TN: Class = 0 and vasospasm is 0

- FN: Class = 0 and vasospasm is 1

Where:

$$\text{Sensibility} = \frac{\text{TP}}{\text{TP} + \text{FN}} \quad (3.16)$$

and

$$\text{Specificity} = \frac{\text{TN}}{\text{TN} + \text{FP}} \quad (3.17)$$

### 3.8. Vasospasm Classifiers

This last section uses again both a Random Forest classifier and a Logistic Regression classifier to predict the likelihood of vasospasm, i.e., to assess Objective 5 (Extended Evaluation) (see 1.6.2.). Input variables include: ‘Patient’, ‘Total Volume (ml)’, ‘Max Slice Thickness’, vasospasm development, the AI-Fisher Modified Scale and age from clinical database. Vasospasm serves as the gold standard for the model.

Both programs performs similarly to the previous classifiers, importing the data frame, the features (X), and the target labels (Y). However, now the target labels are already defined as binary classes (0 and 1). Stratified K-Fold cross-validation with 10 splits is set up to ensure balanced class distribution during training. For each fold, the training data undergoes oversampling using SMOTE to address class imbalance, followed by standardization. Hyperparameters for both the Random Forest and Logistic Regression are optimized using GridSearchCV.

The model’s predictions are evaluated using confusion matrices, classification reports, ROC AUC, and precision-recall AUC metrics, which are averaged and their standard deviations calculated across folds. The feature importance is assessed using permutation importance.

## 4. ANALYSIS OF THE RESULTS

After applying the inclusion and exclusion criteria mentioned in the previous section, a total of 143 subjects were included (Figure 4.1). A total of 55 subjects were excluded due to either a lack of available CT images or death within the first three days of ICU admission. The modified Fisher scale grades assigned to each subject are also depicted, revealing a significant disparity in the distribution among the grades.

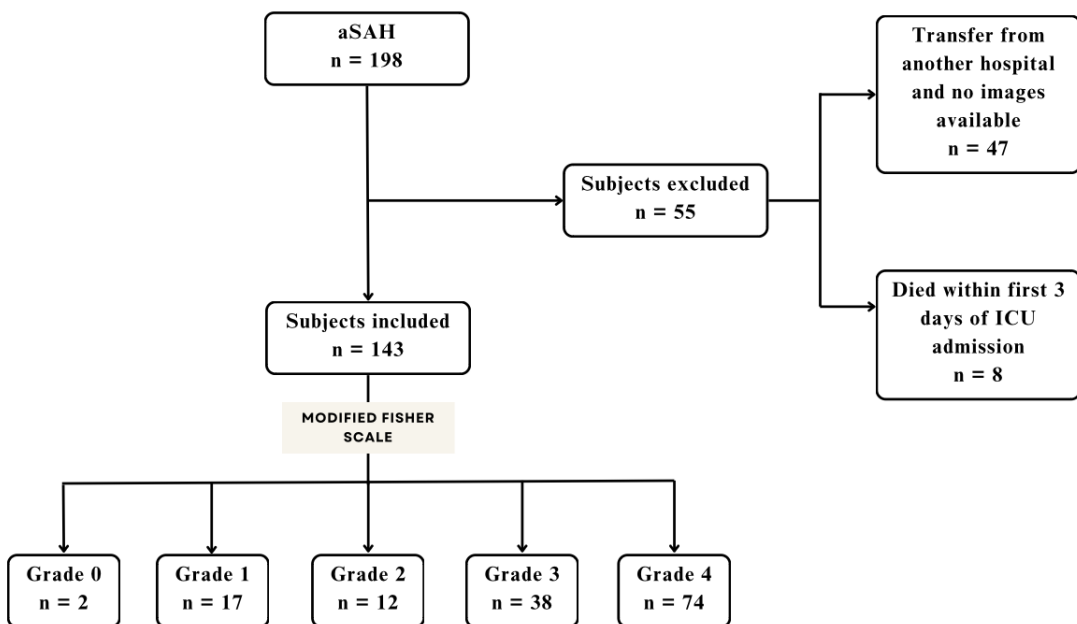


Fig. 4.1. A total of 198 aSAH patients between 2012 and 2023 were retrospectively reviewed. After selection, 143 aSAH patients were included.

### 4.1. Patient Population Results

ICU database for the included subjects is represented in Table 4.1, providing an overview of baseline characteristics, severity scales, treatment and complications of aSAH patients in HUG.

Furthermore, the presence of bleed, IVH and suprasellar cistern bleed variables, all in binary format, were collected from the CT image for all the 143 subjects.

TABLE 4.1. ICU DATABASE: BASELINE CHARACTERISTICS,  
SEVERITY SCALES, TREATMENT AND COMPLICATIONS OF 143  
ASAH PATIENTS.

Baseline characteristics	
<b>Age</b>	57 (13) *
<b>Sex (females)</b>	86 (60)
Severity Scales	
<b>Fisher</b>	
Fisher 1 - 2	43 (30)
Fisher 3 - 4	100 (70)
<b>Hunt and Hess</b>	
Hunt and Hess 1 - 3	96 (67)
Hunt and Hess 4 - 5	47 (33)
<b>GCS</b>	
GCS $\geq$ 8	98 (69)
GCS $\leq$ 8	45 (31)
Treatment	
<b>Nimodipine</b>	140 (98)
Complications	
<b>Vasospasm</b>	
Clinical Vasospasm	19 (13)
TCD Vasospasm	26 (18)
Angiographic Vasospasm	17 (12)
Any Vasospasm	33 (23)
<b>Cerebral Infarction</b>	32 (22)
<b>Rebleeding</b>	11 (8)
<b>Epileptic seizures</b>	10 (7)
<b>Hydrocephalus</b>	53 (37)
<b>Mortality</b>	27 (19)
<b>Total patients</b>	143

Data expressed as N(%)

\* Age expressed as mean  $\pm$  std

## 4.2. Segmentation Results and Final Model

This section explores the results obtained for Objective 1 (Model Development) (see 1.6.2.), where the final model for hemorrhage segmentation is selected based on the performance.

#### 4.2.1. Thresholding-based Segmentation Results

The manually selected threshold value for segmentation was  $T = 180$ . As shown in the histogram from Figure 4.2, the highest concentration of white pixels corresponds to intensity values above 250. However, to account for the presence of diffused blood, which appears as less dense tissue, and to address variability between subjects, a more conservative threshold of  $T = 180$  was chosen. This ensures that the segmentation includes not only the dense hemorrhage regions but also areas with diffused blood.

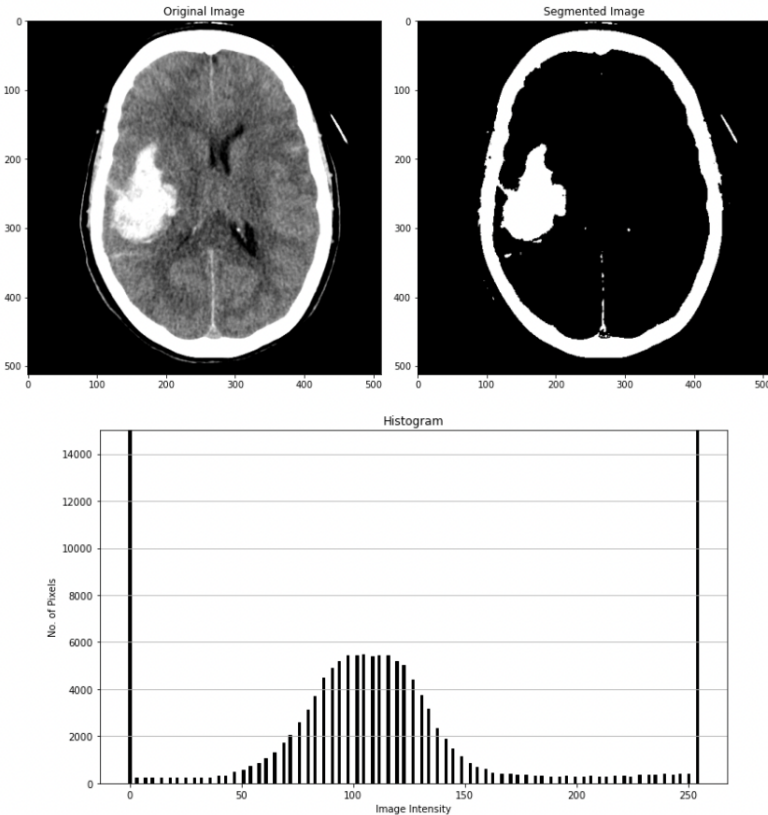


Fig. 4.2. Comparison of Original and Segmented Images with Corresponding Histogram for subject HSA 129. The original CT scan (top left) and its segmented version (top right) highlight the separation of denser tissues from softer tissues using a thresholding-based method. The histogram (bottom) displays the distribution of image intensities.

Nevertheless, while this method effectively differentiates the hemorrhage (higher density) from the rest of the brain (less density), it is not able to separate the bone (high density). Consequently, this leads to errors when computing segment statistics as the bone will also be considered as part of the segment. This method served as a basic approach to the segmentation task, but a more complex model is needed to accurately segment the hemorrhage without the skull. Therefore, this method was discarded.

#### **4.2.2. Automated Segmentation Models Results**

##### **Pre-trained MONAI Tumor Segmentation Model**

To ensure a comprehensive understanding and proper functioning of the MONAI tumor model, the initial approach involved testing the model with the proposed tumor database. The results demonstrated the model's ability to accurately segment the different regions of interest within the tumor with a mean Dice score of 0.8518.

However, when applied directly to hemorrhage CT images, segmentation was not performed successfully as the model was specifically trained for MRI images (Dice score of 0.2759).

Nevertheless, the code from this model proved useful, particularly the pre-processing adjustments that separated the brain from the bone. Adjusting this section minimally for CT contrast allowed for it to be used in U-Net final model.

##### **Final Model: U-Net Segmentation Model**

This model, incorporating some of the pre-processing features from the previous one, was selected as the final choice.

Figure 4.3 illustrates three different examples of segmentation performance, highlighting the model's effectiveness in identifying and segmenting hemorrhages. Each row presents a unique example: the original image, the ground truth mask, the predicted mask, and an overlay of the predicted mask with the ground truth. The IoU and Dice Coefficient values, all above 0.90, indicate high accuracy across all examples.

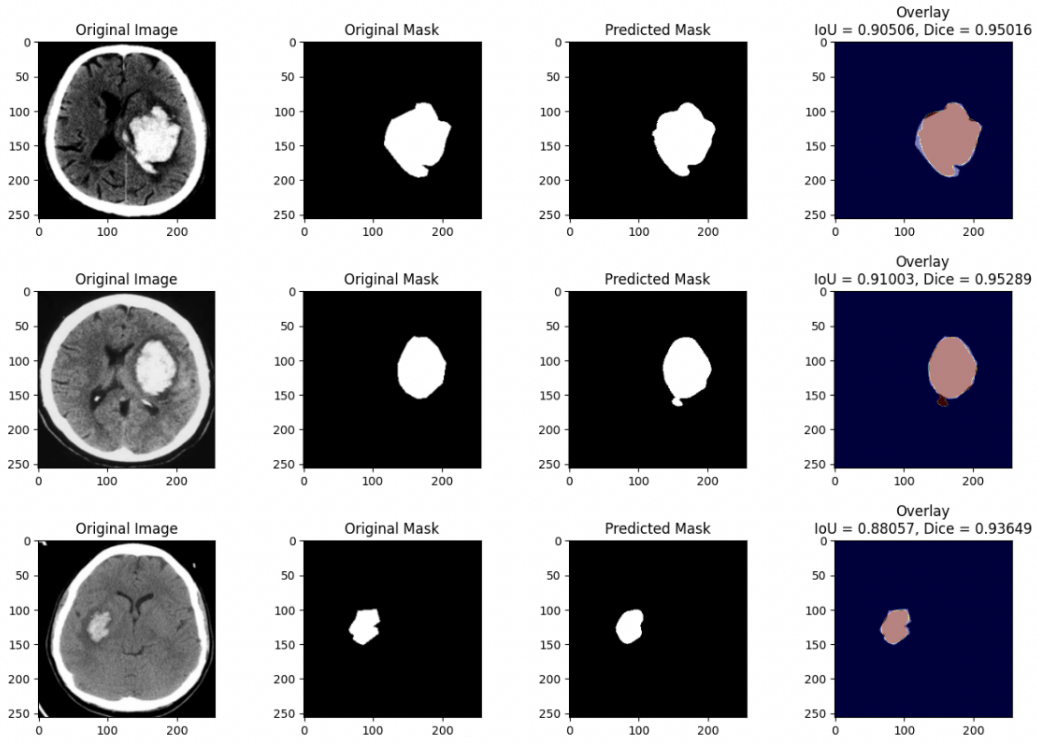


Fig. 4.3. U-Net Model Performance: Each row presents a different example from the validation dataset, comparing the original mask with the predicted mask by the model.

A graphical analysis is shown in Figure 4.4 representing IoU (left) and Dice Coefficient (right) plots.

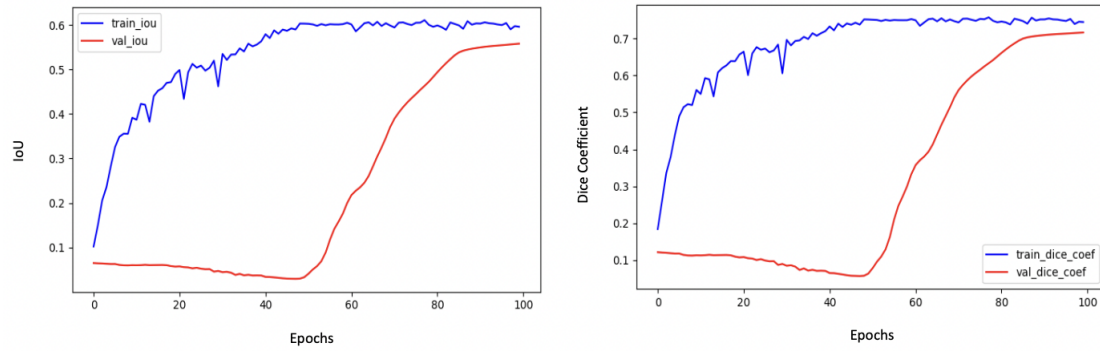


Fig. 4.4. Training and validation performance metrics of the model over 100 epochs, showing the IoU and Dice Coefficient. The graphs indicate high training performance with eventual improvement in validation metrics, demonstrating the model's learning and generalization capabilities. *Legend:* ‘train\_iou’: IoU during training; ‘val\_iou’: IoU during validation; ‘train\_dice\_coef’: Dice Coefficient during training; ‘val\_dice\_coef’: Dice Coefficient during validation

Training and validation loss curves are represented in Figure 4.5.

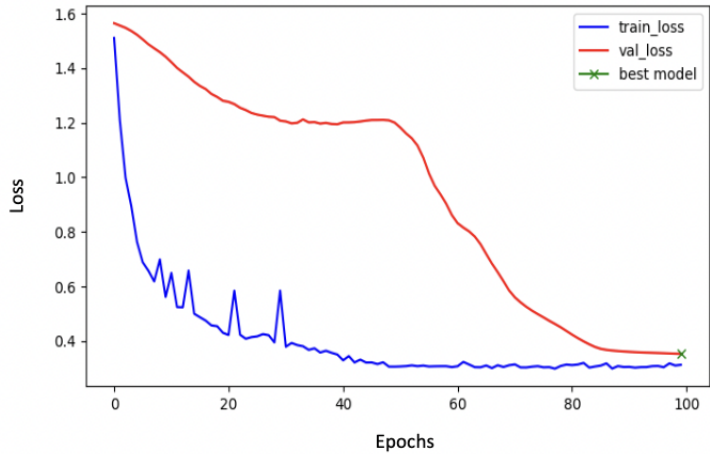


Fig. 4.5. Training and validation loss curves over 100 epochs. The model shows a significant reduction in both training and validation loss, with the best model indicated by the green marker, demonstrating effective learning and generalization. *Legend:* ‘train\_loss’: loss curve for training data; ‘val\_loss’: loss curves for validation data; ‘best model’: best performing trained model

Figure 4.6 shows the segmentation performance when the model is applied to the aSAH database from the HUG in an example of a CT slice from subject HSA 129. Note that this model is applied to all slices from a series with a loop.

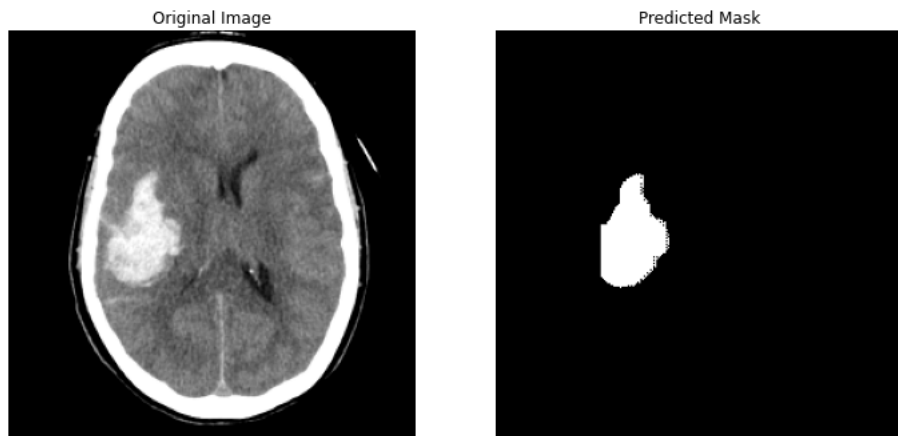


Fig. 4.6. Comparison of an original brain CT image (left) with the predicted segmentation mask (right) generated by the model, illustrating the model’s ability to accurately identify and segment the region of interest.

#### 4.2.3. 3D Slicer Segmentation Results

##### Grow from seeds Results

In Figure 4.7 the results from segmentation using grow from seeds method are presented.

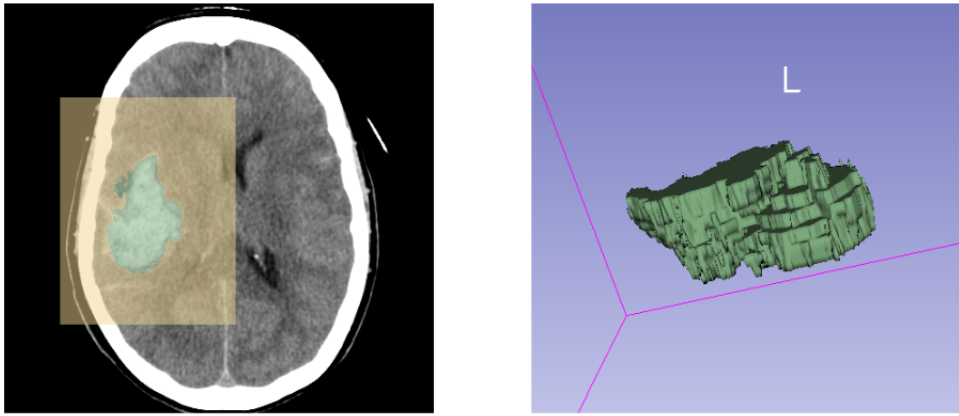


Fig. 4.7. Grow from seeds Segmentation: The image on the left shows the segmented region of interest in green. The right image displays the 3D reconstruction of the segmented area, providing a detailed view of its shape and volume.

### Total Segmentator Extension Results

In Figure 4.8 the results from segmentation using Total Segmentator extension are presented.

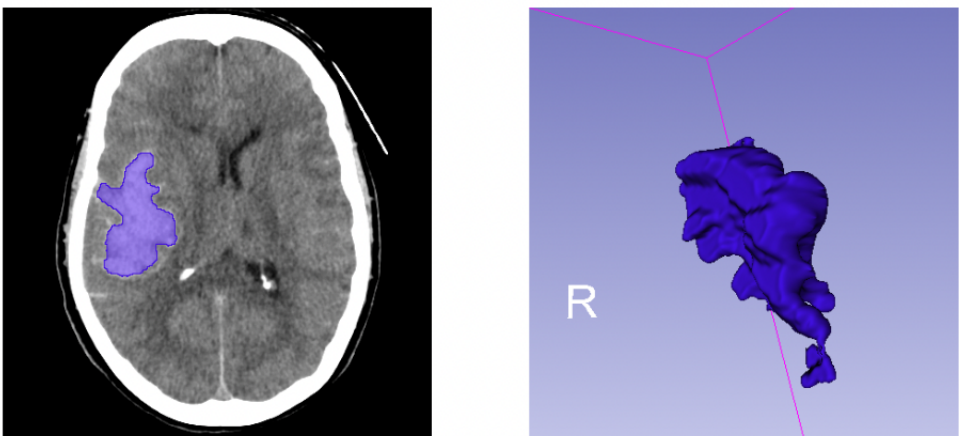


Fig. 4.8. Total Segmentator: The image on the left shows the segmented region of interest in purple. The right image displays the 3D reconstruction of the segmented area, providing a detailed view of its shape and volume.

Overall, **Objective 1 (Model Development) was accomplished** (see 1.6.2.). CT segmentation was performed using the U-Net model with pre-processing from the MONAI model, resulting in a model with high accuracy (Dice Coefficient = 0.95 and IoU = 0.90). This allowed for a precise computation of hemorrhage features, that will be introduced in the classifiers for both modified Fisher scale assignment and the new proposed model for

vasospasm prediction.

### 4.3. Segment Statistics Results

An example is proposed to illustrate segment statistics results. Figure 4.9 presents the section distribution for HSA 129 within the original image and the mask. It can be observed that the highest blood concentration occurs in section (2, 1), representing 71.65% of the total hemorrhage. The total volume obtained was 30.566 ml, with a maximum clot thickness of nine slices. The average density obtained was 81.479 HU. It is important to note that the program operates on the entire volume, whereas in this instance, only two-dimensional slices are being displayed.

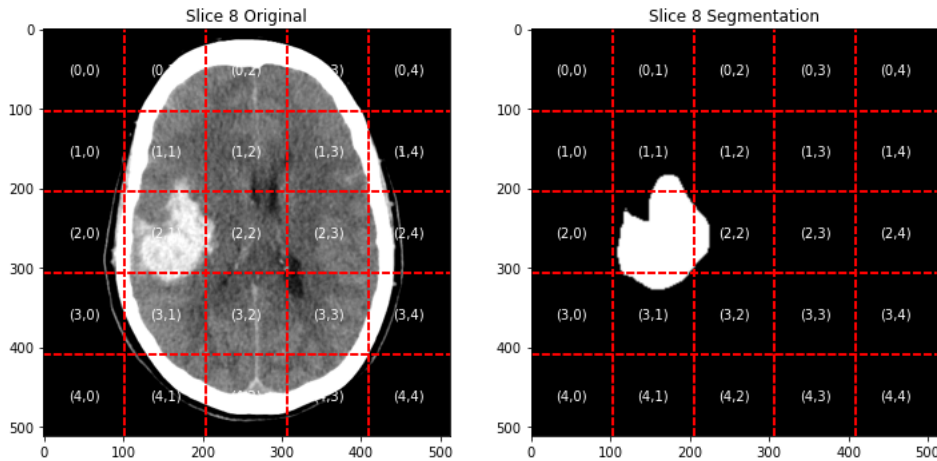


Fig. 4.9. Comparison of Original and Segmented CT Slice: The left image shows the original axial CT slice (HSA 129). The right image displays the corresponding hemorrhage segmented slice, where the region of interest has been effectively isolated.

### 4.4. Modified Fisher Scale Classifier Results

Results for Objective 2 (Automated Scale) (see 1.6.2.) are presented in this section. Firstly, for the binary approach, a basic logistic regression classifier was sufficient to obtain significant results. Figure 4.10 illustrates the model performance metrics for the separation of grade 4 hemorrhages in the modified Fisher Scale. In this context, the ROC AUC is measuring the model's performance to separate the modified Fisher grade 4 from the rest.

Regarding the logistic weights for each value, features with higher positive weight ( $w$ ), that is to say higher feature importance over the model, were: ‘IVH’ with  $w = 2.47 \pm 0.13$ , ‘suprasellar cistern bleed’ with  $w = 0.75 \pm 0.18$  and ‘maximum clot thickness’ with  $w = 0.54 \pm 0.20$ .

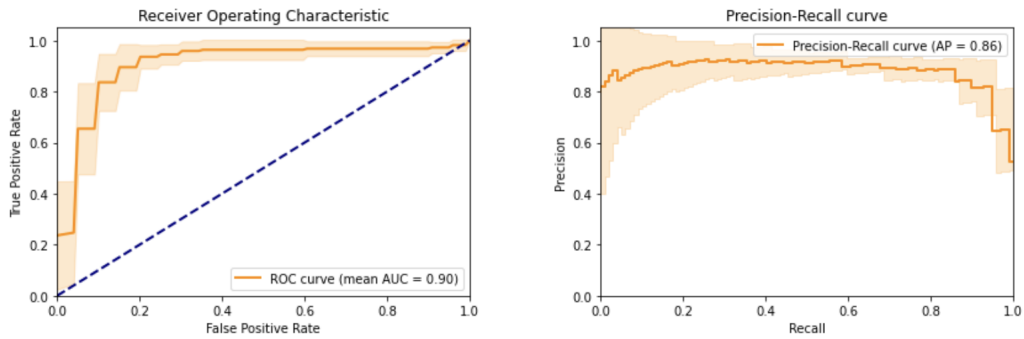


Fig. 4.10. Model Performance Metrics: The ROC curve ( $AUC = 0.90 \pm 0.03$ ) and Precision-Recall curve ( $AP = 0.86 \pm 0.14$ ) demonstrate excellent accuracy and precision in distinguishing grade 4 hemorrhages on the modified Fisher scale.

Conversely, the second grouping option in three classes is evaluated, with regard to the predictive efficacy of logistic regression and random forest classifiers. Following the previously mentioned arrangement (see 3.6.), recall:

- Class 0: Combines grades 0 and 1 (grade 0 vasospasm risk of 0% and grade 1 of 24%)
- Class 1: Combines grades 2 and 3 (both grades present a vasospasm risk of 33%)
- Class 2: Grade 4 (vasospasm risk of 40%)

#### 4.4.1. Random Forest Classifier Results

As shown in Figure 4.11, the initial class distribution was highly imbalanced, with class 2 (corresponding to grade 4) having the highest number of samples. To address this issue, the ADASYN method was employed. ADASYN generates synthetic samples for the minority classes (0 and 1), equalizing the frequency of all classes.

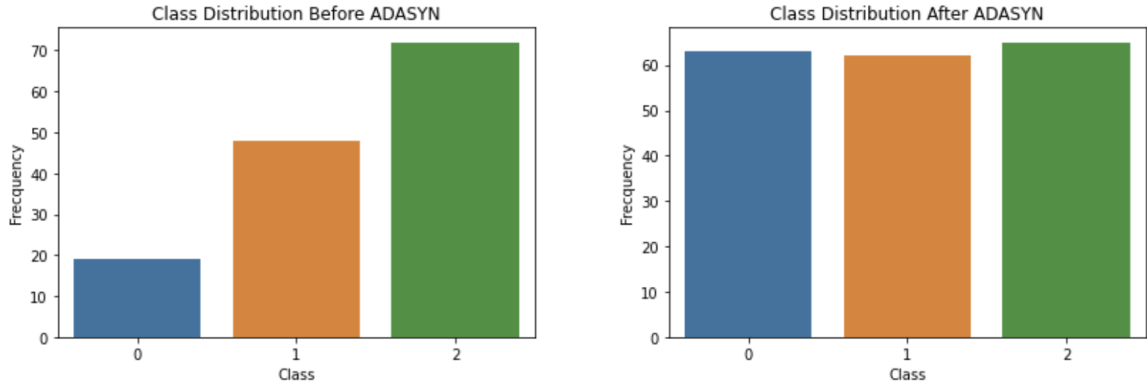


Fig. 4.11. Class distribution before and after applying ADASYN. The left graph shows a highly imbalanced class distribution, while the right graph shows a balanced distribution achieved through adaptive synthetic oversampling with ADASYN.

Regarding the classifier's performance, it is displayed in Figure 4.12. The ROC curves (left plot) illustrate the classifier's performance across different classes:

- Class 0 (Blue Curve): Mean ROC AUC of  $0.89 \pm 0.10$ .
- Class 1 (Orange Curve): Mean ROC AUC of  $0.80 \pm 0.13$ .
- Class 2 (Green Curve): Mean ROC AUC of  $0.95 \pm 0.08$ .

The shaded areas represent the variability of the ROC curves, providing insight into the robustness of the classifier.

On the other hand, the Precision-Recall curves (right plot in Figure 4.12) show the trade-off between precision and recall for each class:

- Class 0 (Blue Curve): Mean Precision-Recall AUC of  $0.65 \pm 0.26$ .
- Class 1 (Orange Curve): Mean Precision-Recall AUC of  $0.73 \pm 0.14$ .
- Class 2 (Green Curve): Mean Precision-Recall AUC of  $0.94 \pm 0.11$ .

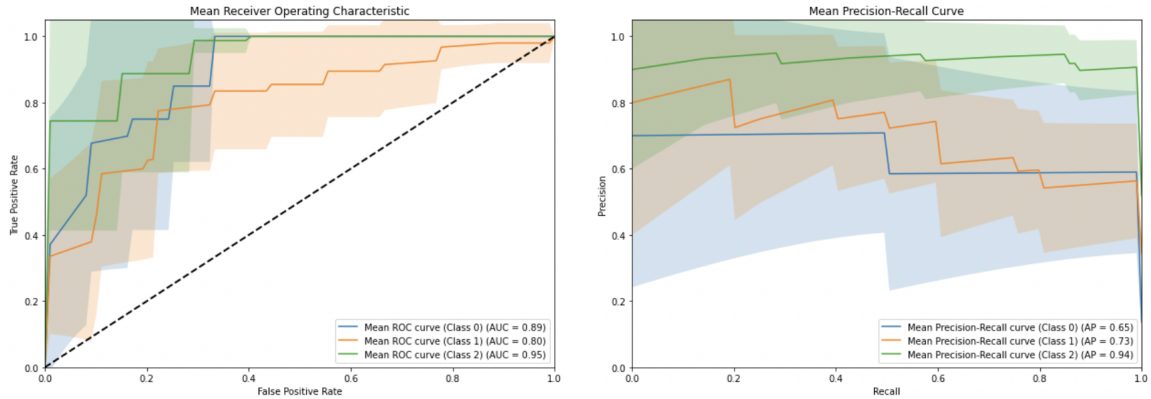


Fig. 4.12. Classifier Performance Metrics. The ROC curves (left) show the classifier's ability to distinguish between classes, with AUC values of 0.89 for class 0, 0.80 for class 1, and 0.95 for class 2. The Precision-Recall curves (right) indicate the reliability of predictions, with AP values of 0.65 for class 0, 0.73 for class 1, and 0.94 for class 2.

Additionally, the confusion matrix is presented in Table 4.2. to evaluate the model.

TABLE 4.2. RANDOM FOREST CONFUSION MATRIX  
(*MEAN*  $\pm$  *STD*)

	<b>Predicted Class 0</b>	<b>Predicted Class 1</b>	<b>Predicted Class 2</b>
<b>Actual Class 0</b>	$1.3 \pm 0.64$	$0.6 \pm 0.66$	$0.0 \pm 0.0$
<b>Actual Class 1</b>	$1.3 \pm 0.64$	$2.4 \pm 0.80$	$1.1 \pm 0.83$
<b>Actual Class 2</b>	$0.0 \pm 0.0$	$0.2 \pm 0.40$	$7 \pm 0.63$

Top influential feature according to feature importance analysis was 'IVH' ( $0.38 \pm 0.10$ ).

#### 4.4.2. Logistic Regression Classifier Results

Class distribution imbalance for the logistic regression classifier was solved using SMOTE, performing similarly as ADASYN (Figure 4.13).

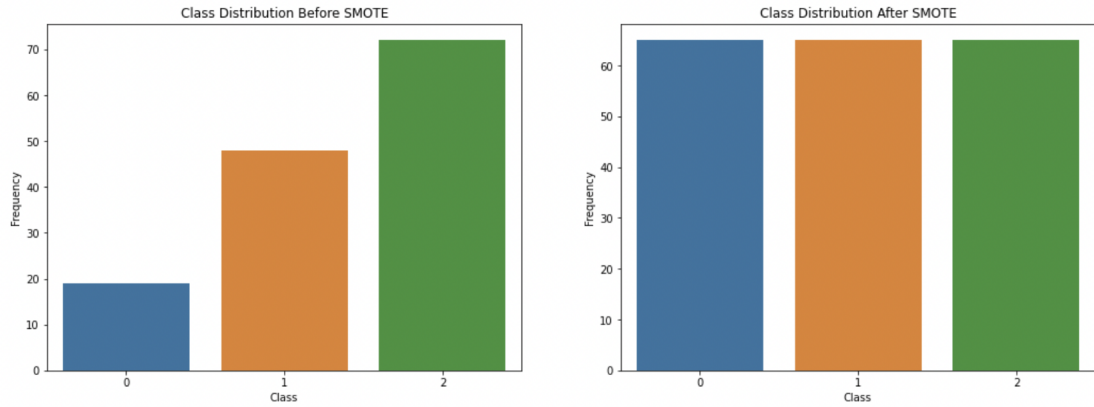


Fig. 4.13. Class distribution before and after applying SMOTE. The left graph shows a highly imbalanced class distribution, while the right graph shows a balanced distribution achieved through adaptive synthetic oversampling with SMOTE.

Regarding the logistic regression classifier's performance, it is displayed in Figure 4.14. Results obtained are highly similar to those from Random Forest classifier. The ROC curves (left plot) illustrate the classifier's performance across different classes:

- Class 0 (Blue Curve): Mean ROC AUC of  $0.84 \pm 0.14$ .
- Class 1 (Orange Curve): Mean ROC AUC of  $0.70 \pm 0.18$ .
- Class 2 (Green Curve): Mean ROC AUC of  $0.88 \pm 0.11$ .

Similarly, Precision-Recall curves (right plot in Figure 4.14) show the trade-off between precision and recall for each class:

- Class 0 (Blue Curve): Mean Precision-Recall AUC of  $0.57 \pm 0.25$
- Class 1 (Orange Curve): Mean Precision-Recall AUC of  $0.65 \pm 0.18$
- Class 2 (Green Curve): Mean Precision-Recall AUC of  $0.87 \pm 0.12$

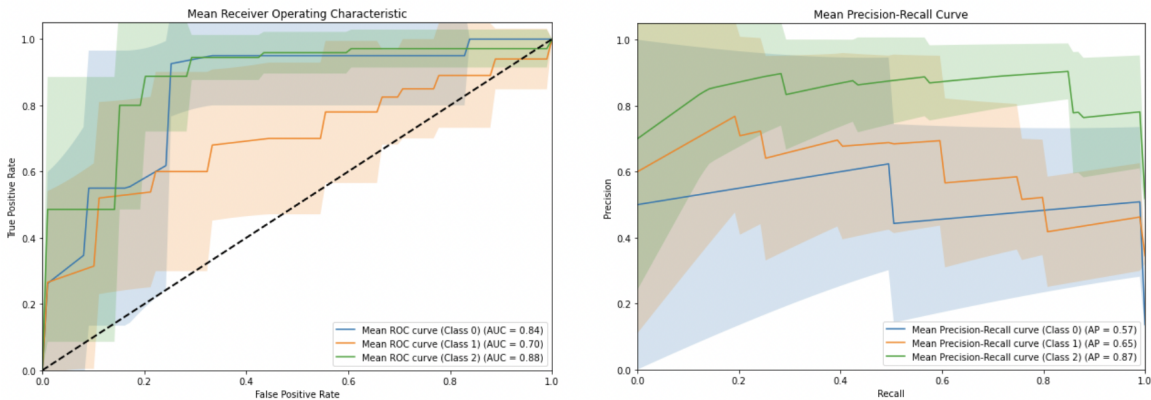


Fig. 4.14. Classifier Performance Metrics. The ROC curves (left) show the classifier's ability to distinguish between classes, with AUC values of 0.84 for class 0, 0.70 for class 1, and 0.88 for class 2. The Precision-Recall curves (right) indicate the reliability of predictions, with AP values of 0.57 for class 0, 0.65 for class 1, and 0.87 for class 2.

The confusion matrix for this model is presented in Table 4.3.

TABLE 4.3. LOGISTIC REGRESSION CONFUSION MATRIX  
(*MEAN*  $\pm$  *STD*)

	<b>Predicted Class 0</b>	<b>Predicted Class 1</b>	<b>Predicted Class 2</b>
<b>Actual Class 0</b>	$0.5 \pm 0.50$	$1.3 \pm 0.78$	$0.1 \pm 0.30$
<b>Actual Class 1</b>	$1.0 \pm 0.89$	$2.6 \pm 1.28$	$1.2 \pm 0.98$
<b>Actual Class 2</b>	$0.1 \pm 0.30$	$0.7 \pm 0.78$	$6.4 \pm 1.20$

Regarding the logistic regression weights (mean  $\pm$  std) analyzed for each class:

- Class 0: Most significant predictors were 'Bleed' with  $w = -1 \pm 1.01$ , 'IVH' with  $w = -3.9 \pm 6.28$ , 'Suprasellar cistern bleed' with  $w = -1.08 \pm 0.25$  and 'Hemorrhage in column 2' with  $w = -1.54 \pm 2.71$ . Note that negative weights indicate an inverse relationship between the predictor variables and the outcome.
- Class 1: Most significant positive predictors were 'Bleed' with  $w = 0.55 \pm 0.39$  and 'Hemorrhage in column 2' with  $w = 0.59 \pm 0.62$ .
- Class 2: Most significant predictors were 'IVH' with  $w = 4.42 \pm 4.93$ , 'Max Slice Thickness' with  $w = 2.07 \pm 4.32$  and 'suprasellar cistern bleed' with  $w = 0.86 \pm 0.46$ .

As for this application the Random Forest classifier presents better results, it is the final selected model.

Therefore, **Objective 2 (Automated Scale) is achieved** (see 1.6.2.) by successfully assigning the modified Fisher scale with accurate performance metrics using the Random Forest classifier: higher risk of vasospasm - grade 4 (mean ROC AUC of  $0.95 \pm 0.08$ ), moderate risk of vasospasm - grades 2 and 3 (mean ROC AUC of  $0.80 \pm 0.13$ ) and lower risk of vasospasm - grades 0 and 1 (mean ROC AUC of  $0.89 \pm 0.10$ ).

#### 4.5. Variability Results

The objectives associated with these results are Objective 3 (Variability Assessment) and Objective 4 (Predictive Evaluation) (see 1.6.2.). The percentage of differences between the assessment of both neuroradiologists was of 2.67% and the Kappa coefficient obtained was 0.95, representing almost perfect agreement between both neuroradiologists.

For the multivariable models, Kappa coefficient between the automated modified Fisher scale by logistic regression model and the modified Fisher scale assigned by neuroradiologist 1 is of 0.539, and Kappa coefficient between the automated modified Fisher scale and the modified Fisher scale assigned by neuroradiologist 2 is of 0.524, both moderate. That is an average percentage of error of 28.1%.

Regarding vasospasm prediction:

- Modified Fisher Scale by neuroradiologist 1:
  1. Class 2 (grade 4) and Class 0 (grades 0 and 1): sensitivity of 95.65% and specificity of 26.47%.
  2. Class 1 (grades 2 and 3) and Class 0 (grades 0 and 1): sensitivity of 91.67% and specificity of 32.73%.
- Modified Fisher Scale by neuroradiologist 2:
  1. Class 2 (grade 4) and Class 0 (grades 0 and 1): sensitivity of 91.67% and specificity of 27.69%.
  2. Class 1 (grades 2 and 3) and Class 0 (grades 0 and 1): sensitivity of 83.33% and specificity of 31.03%.
- Modified Fisher Scale by AI model (logistic regression model):
  1. Class 2 (grade 4) and Class 0 (grades 0 and 1): sensitivity of 80% and specificity of 16.67%.
  2. Class 1 (grades 2 and 3) and Class 0 (grades 0 and 1): sensitivity of 77.78% and specificity of 27.27%.

## 4.6. Vasospasm Classifiers Results

For the final Objective 5 (Extended Evaluation) (see 1.6.2.), both Random Forest and Logistic Regression models (with input variables the modified Fisher scale, the hemorrhage's volume, thickness and patient's age) are evaluated.

### 4.6.1. Random Forest Classifier Results

Figure 4.15 represents the Random Forest classifier performance for the prediction of vasospasm. The mean ROC AUC obtained is  $0.67 \pm 0.13$  and the mean Precision-Recall AUC is  $0.68 \pm 0.17$ .

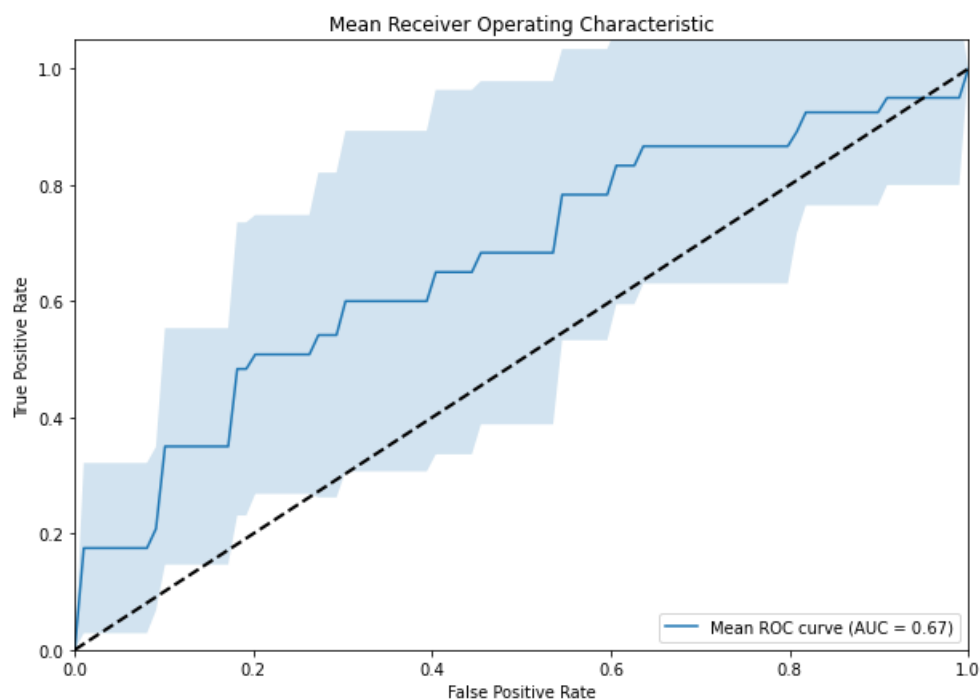


Fig. 4.15. Classifier Performance Metric ROC curve. The mean AUC value for vasospasm classifier is 0.67.

The confusion matrix is presented in Table 4.4., showing a higher accuracy in predicting the absence of vasospasm compared to the presence of vasospasm.

TABLE 4.4. RANDOM FOREST CONFUSION MATRIX FOR  
VASOSPASM ( $MEAN \pm STD$ )

		<i>Predicted</i>	
		No Vasospasm	Vasospasm
<i>Real</i>	No Vasospasm	$8.6 \pm 1.02$	$1.9 \pm 1.04$
	Vasospasm	$2.2 \pm 1.05$	$1.2 \pm 0.84$

The model predicted vasospasm with a sensitivity of  $0.81 \pm 0.25$  and a specificity of  $0.54 \pm 0.23$ .

Top feature importance for vasospasm classification was ‘Total Volume (ml)’ ( $0.02 \pm 0.01$ ).

#### 4.6.2. Logistic Regression Classifier Results

Figure 4.16 represents the Logistic Regression classifier performance for the prediction of vasospasm. The mean ROC AUC obtained is  $0.69 \pm 0.16$  and the mean Precision-Recall AUC is  $0.57 \pm 0.13$ .

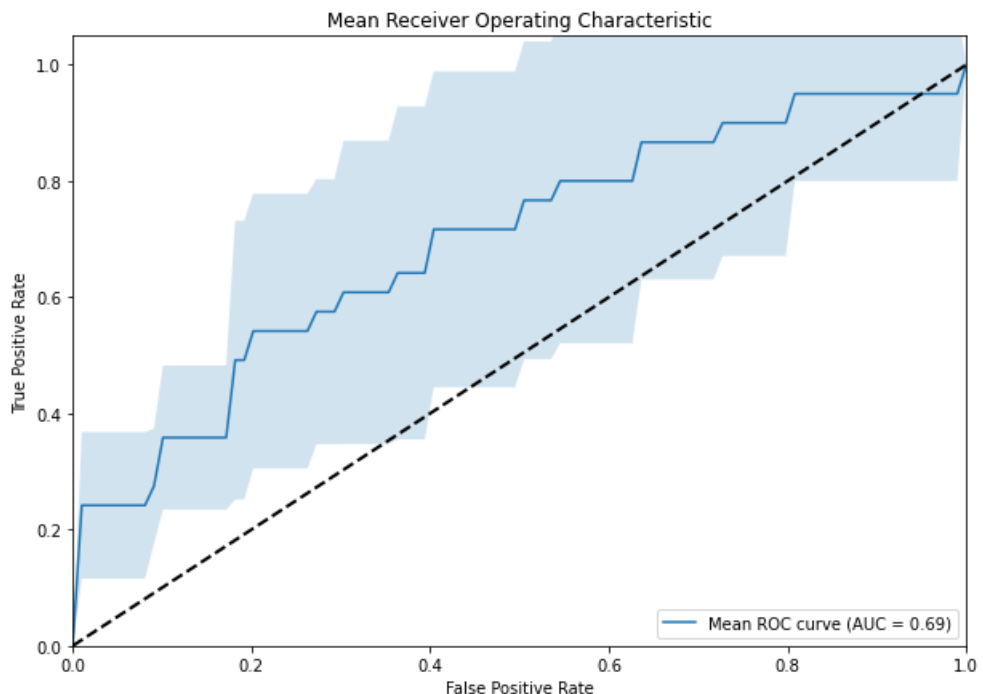


Fig. 4.16. Classifier Performance Metric ROC curve. The mean AUC value for vasospasm classifier is 0.69.

The confusion matrix is presented in Table 4.5.

TABLE 4.5. RANDOM FOREST CONFUSION MATRIX FOR VASOSPASM ( $MEAN \pm STD$ )

		<i>Predicted</i>	
		No Vasospasm	Vasospasm
<i>Real</i>	No Vasospasm	$6.0 \pm 2.10$	$4.5 \pm 2.09$
	Vasospasm	$1.10 \pm 0.90$	$2.3 \pm 0.83$

The model predicted vasospasm with a sensitivity of  $0.87 \pm 0.23$  and a specificity of  $0.67 \pm 0.18$ .

The feature with highest logistic regression weight was ‘Age’ with  $w = 0.03 \pm 0.05$ , followed by ‘Total Volume (ml)’ with  $w = 0.02 \pm 0.06$ .

Contrary to the modified Fisher scale assignment (for which the Random Forest approach showed higher AUC), in this case better classification results are presented by the logistic regression model. Therefore, **Objective 5 (Extended Evaluation) is completed** by creating a new assessment method derived from the modified Fisher scale, incorporating radiological and demographic features such as volume, thickness and age (see 1.6.2.).

## 5. DISCUSSION OF THE RESULTS

The results of this study highlight significant advances and challenges in the segmentation of aSAH and the classification of risk scales and vasospasm onset, while providing a comprehensive understanding of the efficacy and limitations of the different models and techniques used. Overall, the results presented here represent a substantial advancement in the management of aSAH patients, leading to improved outcomes.

### 5.1. Segmentation

#### 5.1.1. Thresholding-based Segmentation

The thresholding-based segmentation method effectively separates denser tissues from softer tissues, as shown in the histogram (Figure 4.2). However, more advanced techniques are required to precisely extract the bone and isolate only the hemorrhage section for accurate analysis.

#### 5.1.2. Automated Segmentation Models

##### Pre-trained MONAI Tumor Segmentation Model

The Dice score of 0.2759 implied minimal coincidence between the region of interest and the predicted mask due to the different nature of the images. MRI and CT capture different tissue properties: MRI relies on magnetic resonance signals sensitive to water and fat content, providing high contrast for soft structures, while CT uses X-rays to measure tissue density, effectively visualizing bone structures and detecting acute hemorrhages. These fundamental differences in imaging modalities mean that models trained on MRI may not generalize well to CT due to the distinct properties of the images. Additionally, the contrast and texture characteristics in MRI and CT differ significantly. A model trained on MRI may not recognize the same features in CT because tissues and structures appear differently. Therefore, this MONAI model approach ended up not being feasible for non-contrast CT segmentation.

Although it is technically possible to adapt the MRI model to CT features in time-consuming process, it was not worthwhile. The Dice coefficient for the original MRI model, was not higher than the final Dice coefficient achieved by the second proposed U-Net model, which was specifically designed to train on CT images.

Only the section destined to separate the brain from the bone was adapted and used for this application.

## **Final Model: U-Net Segmentation Model**

In Figure 4.3, the IoU and Dice Coefficient values for the examples presented are all above 0.90, indicating high accuracy across all examples and demonstrating the model's robustness and precision.

The graphical analysis shown in Figure 4.4 representing IoU (left) and Dice Coefficient (right) plots can be analyzed as follows:

1. IoU Plot: The IoU for the training data shows a significant increase early in the training process, stabilizing around 0.6, which indicates the model's accuracy in predicting the segmentation mask. On the other hand, the validation IoU remains low initially, indicating poor performance, but improves drastically after epoch 50, aligning closer to the training IoU towards the end.
2. Dice Coefficient Plot: The Dice Coefficient for the training set increases similarly to the IoU, reaching around 0.7, reflecting good performance in segmentation tasks. The validation Dice Coefficient shows a delayed improvement, similar to the IoU, but eventually converges towards the training Dice Coefficient values, suggesting enhanced model performance on unseen data.

Training and validation loss curves are represented in Figure 4.5. The training loss curve (blue) decreases sharply initially and then plateaus, indicating the model is learning and minimizing error on the training data. Additionally, the validation loss (red) decreases more gradually and continues to decline until it reaches a low point at around epoch 90, suggesting the model is generalizing better over time. Finally, the green cross marks the point where the model achieved the best performance on the validation set.

### **5.1.3. 3D Slicer Segmentation**

Using 3D Slicer provided a visual interpretation of the hemorrhage dimensions. However, this approach was less efficient computationally. For a reduced number of subjects, it would have been the best option.

#### **Grow from seeds**

As seen in Figure 4.7, the segmented region (highlighted in green) is well-defined within the background (orange area) on the left image (axial CT for subject HSA 129). Therefore, this tool successfully isolated the region of interest, representing the hemorrhage.

Additionally, a 3D reconstruction of the segmented area is presented. The shape and volume of the segmentation are clearly visible, which is useful for further analysis and understanding the spatial extent of the region.

Note that the quality of the initial seed selection and parameter settings for this method can significantly influence the outcome.

## Total Segmentator Extension

The Total Segmentator Extension produced more accurate segmentation outputs compared to the previous method, though it required greater computational resources. As shown in Figure 4.8 (axial CT for subject HSA 129), the region of interest is effectively isolated. Additionally, the 3D visualization presents smoother boundaries, resulting in a more realistic and precise representation of the hemorrhage.

Finally, the segmentation objective was feasible using the U-Net model combined with pre-processing from MONAI. This allowed to distinguish the region of interest, i.e. the hemorrhage, from the rest of the image with a Dice score and IoU over 90%, and a computation cost achievable with the personal computer. Thus, Objective 1 (Model Development) (see 1.6.2.) is completed with success.

Previous studies, as the one by Inkeaw *et al.* [72], aimed to perform cerebral bleed segmentation also on CT images with deep learning techniques based on region growing, but obtaining median Dice similarity coefficients around 0.37 for each hemorrhage subtype. This score was raised by Nijiati *et al.* [73] with their novel symmetric Transformer network, obtaining a Dice coefficient of  $0.716 \pm 0.031$ .

Therefore, the segmentation approach used in this thesis represents a significant improvement, specially in aSAH automatic segmentation techniques, yielding much higher Dice score values than the ones from the state of the art.

## 5.2. Segment Statistics

The various programs for computing volume, clot thickness and density, as well as the localization program, were found to perform as expected, providing reasonable values for each feature.

Given the absence of standardized measurements in this section, a manual analysis was performed to ensure the accuracy of the computed values. Hemorrhage volume varied from 0 ml (indicating no bleeding) to 85 ml (the largest hemorrhage recorded). Initially, subjects with a volume of 0 ml were scrutinized to confirm the absence of hemorrhage. Subsequently, a parallel verification process was conducted for cases with higher volumes to ascertain the model's effectiveness. Similarly, for the thickness extent, a validation was manually conducted by counting slices with blood presence in each subject. Furthermore, density values were addressed by pixel intensities, where lower intensity hemorrhage corresponded to a lower density. Finally, hemorrhage localization grid was displayed alongside the original image for each slice, allowing for visual confirmation of whether the hemorrhagic mask regions aligned with the sections from original slice.

### **5.3. Modified Fisher Scale Classifier**

Figure 4.10 illustrates the results of the grouped approach to separating grade 4 from the rest using a logistic regression classifier. The ROC curve on the left shows an AUC of  $0.90 \pm 0.03$ , indicating excellent discrimination ability. The precision-recall curve on the right, with an average precision (AP) of  $0.86 \pm 0.14$ , demonstrates the model's high precision and recall in identifying grade 4 hemorrhages.

In regard to the logistic weights, it was expected that feature 'IVH' presents the higher significance. From definition (see Table 1.1) grade 4 in the modified Fisher Scale implies a thick cisternal clot with IVH.

Being able to separate cases with higher risk of vasospasm so accurately represents a significant advancement in patient care and clinical decision-making, enabling more timely and targeted interventions that can improve patient outcomes and reduce complications associated with aSAH.

#### **5.3.1. Random Forest Classifier**

Figure 4.12 presents ROC and Precision-Recall curves to show Random Forest classifier performance. For the ROC curves, class 0 (blue curve) (see 3.6.) achieved a mean ROC AUC of  $0.89 \pm 0.10$ , indicating a high level of accuracy in distinguishing class 0 from other classes. Class 1 (orange curve) had a mean ROC AUC of  $0.80 \pm 0.13$ , which is slightly lower than class 0, suggesting some challenges in accurately classifying this class. Finally, class 2 (green curve) achieved the highest mean ROC AUC of  $0.95 \pm 0.08$ , reflecting excellent classifier performance for this class. Additionally, the Precision-Recall curves show that class 0 had moderate performance (AUC  $0.65 \pm 0.26$ ) with high variability, class 1 performed better (AUC  $0.73 \pm 0.14$ ), and class 2 had the highest performance (AUC  $0.93 \pm 0.11$ ), indicating a strong balance between precision and recall.

Therefore, the model can identify with a significant level of accuracy those cases representing a lower risk of vasospasm and complications (class 0 - grades 0 and 1 in modified Fisher Scale). In clinical practice, this is interesting as it allows physicians to confidently identify patients at lower risk and tailor their treatment accordingly. Moreover, cases with intermediate risk of complications (class 1 - grades 2 and 3 in modified Fisher Scale) are classified moderately good. Finally, highest risk of severe complications (class 2 - grade 4 in modified Fisher Scale) are again perfectly identified, suggesting the need of intense monitoring and early interventions.

The confusion matrix in Table 4.1 provides an overview of the Random Forest model's classification performance. For actual class 0, the model often predicts it as class 0 with a mean of  $1.3 \pm 0.64$ , but there is some misclassification as class 1. For actual class 1, the predictions are distributed with the majority correctly classified as class 1 (mean of  $2.4 \pm 0.8$ ), though there is notable misclassification into class 0 and class 2. For actual class

2, the model performs well, correctly predicting this class with a mean of  $7 \pm 0.63$ , with minimal misclassification.

The results obtained not only demonstrate the classifier's effectiveness in terms of statistical metrics but also underscores its clinical relevance.

### 5.3.2. Logistic Regression Classifier

The performance of the logistic regression classifier, as displayed in Figure 4.14, shows results similar to those of the Random Forest classifier. For the ROC curves, class 0 (blue curve) achieved a mean ROC AUC of  $0.84 \pm 0.14$ , indicating good accuracy in distinguishing class 0. Class 1 (orange curve) had a mean ROC AUC of  $0.70 \pm 0.18$ , which is lower, suggesting some challenges in accurately classifying this class. Lastly, Class 2 (green curve) achieved a mean ROC AUC of  $0.88 \pm 0.11$ , showing strong performance for this high-risk category. Similarly, the Precision-Recall curves show moderate performance with high variability for class 0, better and less variable performance for class 1, and the highest, most balanced performance for class 2.

The confusion matrix in Table 4.2 for the logistic regression model provides insights into the model's classification accuracy for each class. The model shows variability in correctly predicting actual class 0, with a mean of  $0.5 \pm 0.5$  for predicted class 0, and confusion between classes 0 and 1, with predicted class 1 having a mean of  $1.3 \pm 0.78$ . Actual class 1 is most frequently predicted as class 1, with a mean of  $2.6 \pm 1.28$ , but there is notable misclassification into class 0 and class 2. For actual class 2, the model accurately predicts this class with a mean of  $6.4 \pm 1.2$ , although some instances are misclassified as classes 0 and 1.

As expected, logistic regression weights with highest influence for class 0 are negative values related with bleed presence, indicating an inverse relationship between these predictor variables and the outcome. Conversely, most significant predictors for class 1 include positive weights for bleed presence features. Class 2 most significant predictors are again 'IVH' and 'Max Slice Thickness', following the real definition of the grade.

Overall, the random forest classifier performance surpasses the logistic regression classifier for this purpose, achieving ROC AUC curves over 80% for all classes.

The automatically modified Fisher assignment, as well as other risk scores related with the prediction of vasospasm, has not been explored yet in literature. Therefore this thesis represents a novel research line of AI severity score assignments, specially for aSAH outcomes.

## 5.4. Variability

Results obtained in this section suggest that while the automated model shows some ability in replicating human assessments, there is still a notable gap in accuracy and reliability. The moderate Kappa coefficients (both around 0.5) imply that the model may need further refinement and validation to achieve a level of performance comparable to experienced neuroradiologists. Nevertheless, this project establishes a solid basis for future advancements through the incorporation of more sophisticated classification techniques.

Regarding vasospasm predictive value of each provided scale, AI assignment (logistic regression model) shows comparable results to the manual assignment ones. However, AI assignment presents slightly lower values for sensitivity and specificity, suggesting again that future evolution of the model into more complex machine learning techniques is precised, as well as an extended and uniform database.

## 5.5. Vasospasm Classifiers

On the one hand, the Random Forest classifier shows moderate effectiveness in predicting vasospasm, with an ROC AUC of 0.67 and Precision-Recall AUC of 0.68 (Figure 4.15). The confusion matrix (Table 4.3) indicates better performance in predicting the absence of vasospasm, while the true positives (vasospasm) are less accurately predicted.

On the other hand, the Logistic Regression classifier shows moderate effectiveness in predicting vasospasm, with a slightly better ROC AUC (0.69) (Figure 4.16 ) compared to the Random Forest model. However, the Precision-Recall AUC is relatively low (0.52), indicating challenges in accurately predicting the positive class. The confusion matrix reveals a higher number of false positives, which could be problematic in clinical settings.

Feature importances with such small values of significance imply low individual influence of each feature.

Finally, in both cases the overall variability in performance indicates that the models' predictions are not consistently reliable, suggesting a need for further model refinement or alternative modeling approaches to improve accuracy and robustness.

Nevertheless, when these results were compared with current risk scales, the AI model showed improvement. Regarding the two most common scales, the Fisher scale (AUC of 0.545, sensitivity of 84.6% and specificity of 36.6%) and the modified Fisher scale (AUC of 0.617, sensitivity of 85.1% and specificity of 50.4% ), a model able to predict vasospasm with an AUC of 0.69, sensitivity of 87% and specificity of 67% is significant.

Moreover, this thesis is also a breakthrough in this aspect, as only a few machine learning models have been explored for the prediction of vasospasm in literature. A comparable example to this model is found in the paper by Ramos *et al.* [57], in which another logistic regression model is created to predict DCI from known clinical predictors obtain-

ing an AUC of 0.63. Furthermore, they also developed a more advanced machine learning model using all clinical variables, yielding an AUC of 0.68. As observed, the vasospasm prediction model presented in this thesis surpasses comparable studies conducted on the past.

## **5.6. Relevance of the Thesis**

The incidence of aSAH has been increasing over time. In the last 11 years, 198 cases of aSAH have been treated at HUG, of which 13% suffered clinical vasospasm, 20% had a cerebral infarction and 17% of patients died. However, early prediction of vasospasm can significantly reduce neurological deficits and improve patient's outcomes.

In this aspect, the presented thesis is not only important for the potential in reducing hospital costs, but also for improving life's quality of the affected patients. Moreover, by providing physicians accurate and reliable AI tools their diagnosis could be supported by an AI proposal, resulting in a more specific course of treatment for each case.

Finally, this thesis represents a substantial advancement in the use of AI for medical purposes, proving that it is indeed feasible to enhance manual measurements and accurately assign risk scales.

## **5.7. Limitations and Possible Improvements**

As with all research, this study has limitations. To begin with, the final number of subjects included in the project ( $n = 143$ ) and the imbalance between classes for the modified Fisher Scale represented a limitation in both segmentation and classification models. The participants included were all from the same ICU and this may not be representative of cases diagnosed with aSAH in general. Future studies should include subjects from other hospitals to maintain the continuity of this research. Furthermore, another important bias was the data imbalance between modified Fisher scale grades (the vast majority were grade 4 cases) and the lack of uniformity in the data acquisition process, resulting in subjects with different CT image acquisition characteristics. This made data processing and analysis difficult. Furthermore, the final number of cases was not sufficient for a robust machine learning process, and although various data augmentation techniques were used, an expanded database should be considered for future studies. In terms of classification models, those used in this study represent a first basic approach to check the feasibility of the study. Nevertheless, future projects could implement advanced classification models using more complex deep learning techniques to obtain better results. This thesis provides a solid foundation for future research, suggesting that meaningful conclusions can be drawn from AI models in aSAH context.

## **6. REGULATORY FRAMEWORK**

A detailed document outlining the different steps of the project and clarifying data management procedures was submitted for approval to the Comité de Ética de la Investigación con medicamentos (CEIm) at Hospital Universitario de Getafe before starting the study. This document included the different regulations and laws that the project adhered to.

The project was conducted following bioethical regulations, including the Declaration of Helsinki, the Belmont Report, the Oviedo Convention on Human Rights, Law 14/2007 of July 3rd on Biomedical Research, and European legislation on data protection. Specifically, it adhered to Organic Law 3/2018 of December 5th on Personal Data Protection and Guarantee of Digital Rights, Royal Decree 1720/2007, and Law 41/2002 of November 14th on the basic regulation of patient autonomy and obligations regarding clinical information and documentation.

The clinical data and image files used on the study underwent pseudonymization, generating two new datasets: the pseudonymized information used for data analysis, and the additional information that allows for the reversal of anonymization. This additional information was stored in a protected access Excel file held only by the researcher Dr. José A. Lorente on a computer terminal from the HUG. For the image files, the file was kept by Dr. Jorge Sánchez Reyes from the Radiodiagnosis Service. Since the study is retrospective, the non-mandatory nature of obtaining informed consent was requested.

The research required the collection of clinical information from the Hospital Information System (HCIS). Access to the HCIS was always carried out by a hospital physician.

This thesis is covered by the Creative Commons License.

## **7. SOCIOECONOMIC IMPACT**

### **7.1. Impact on the National Health System**

Automating the modified Fisher scale assignment has the potential to improve efficiency and accuracy in healthcare, reduce costs, increase access to quality diagnostics, promote medical research, and enhance patients' quality of life, all of which can contribute positively to socio-economic development.

While AI is not intended to replace the manual evaluations performed by neuroradiologists, it can provide a valuable second opinion, helping to reduce interrater variability. This would be particularly significant in situations where physicians are experiencing stress and fatigue during on-call shifts. Furthermore, improved efficiency in diagnostics and treatments can imply a better allocation of the hospital resources, thus lowering the total healthcare costs. The availability of an automated tool can facilitate large-scale studies on aSAH, providing consistent and high-quality data for future research.

On the other hand, the ability to accurately predict the onset of vasospasm would lead to early diagnosis, improving health outcomes and quality of life for patients through better defined courses of treatments. It would also reduce significantly ICU stay and, as a consequence, it would reduce hospital costs. Approximately, a day in the ICU costs around 2,100 € per patient and the average stay for aSAH patients in the ICU from the HUG is of 10 days. Therefore, 21,000 € are destined for each aSAH patient during their ICU stay (without considering additional clinical tests, surgical procedures or radiological scans). In the hypothetical scenario where early prediction of vasospasm leads to a reduction of 3 days in ICU stay, the approximate cost savings would amount to 6,300€ per patient. Considering 198 aSAH patients were admitted between 2012 and 2023, an average of 18 aSAH patients entered the ICU per year. Overall, the total annual hospital cost for aSAH patients would be reduced 113,400 € with this project.

### **7.2. Project Resources**

The development of this thesis required a variety of personal, informational and computational resources.

The collaboration within institutions is supported by an active agreement between the HUG and the Universidad Carlos III de Madrid (UC3M).

The research team members contributing to this project included: Dr. José Ángel Lorente, Dr. Jorge Mario Sánchez, Dr. Eva Tejerina, Prof. Pablo Martínez and Prof. Matilde Pilar Sánchez. The project is aligned with existing research lines at HUG (sepsis biomarkers, diagnosis and treatment of SAH, and pathophysiology and diagnosis of

COVID-19 related acute respiratory failure) in the Intensive Care Medicine and Radiodiagnostic Services.

### 7.2.1. Human Resources

Both Dr. José Ángel Lorente and Prof. Matilde Pilar Sánchez served as tutors for this thesis. Along with Prof. Pablo Martínez, they provided meaningful insights and guidance throughout the various stages of the project. Collaborators from HUG included Dr. Eva Tejerina from the ICU, who provided the clinical database and information about previous studies, and Dr. Jorge Mario Sánchez from the Radiology service, who supplied the CT images and highlighted important features. Whenever obstacles were faced, all collaborators were quick to offer their assistance. Table 7.1. illustrates the approximate cost per hour for human supply (data from the Instituto Nacional de Estadística (INE) [74]).

TABLE 7.1. COST BREAKDOWN OF HUMAN RESOURCES

Resource	Cost/Time (€/hours)	Time (hours)	Total Cost (€)
HUG Tutor	17.7	50	885
UC3M Tutor	17.7	30	531
HUG Collaborators	17.7	10	177
UC3M Collaborator	17.7	30	531
Student	10	900	9,000
<b>Total:</b>			11,124

### 7.2.2. Material Resources

Materials employed for the thesis include the student's personal computer, which used for running the different programs on the CPU. As Python is an open code programming language, no licenses were required. CT images acquisition costs are also considered (140 € per image) [75]. As 143 patients were included in the study, 20,020 € were destined to image acquisition.

An approximate material cost is presented in Table 7.2.

TABLE 7.2. COST BREAKDOWN OF MATERIAL RESOURCES

Resource	Cost/Time (€/year)	Time (months)	Total Cost (€)
Personal Computer	250	10	208.3
Image Acquisition	-	-	20,020
<b>Total:</b>			20,228.3

### 7.2.3. Total Cost

The approximate total cost for the thesis is broke down in Table 7.3.

TABLE 7.3. COST BREAKDOWN OF TOTAL RESOURCES

Resource	Total Cost (€)
Human Resources	11,124
Material Resources	20,228.3
<b>Total:</b>	31,352.3

## 8. CONCLUSION AND FUTURE STEPS

This thesis focused on the automated modified Fisher Scale assignment using CT image features extracted by advanced segmentation techniques, followed by the development of a classifier to predict vasospasm. The theoretical background and state of the art from the systematic review, served as motivation supporting the hypothesis of the need of new avenues to manage aSAH patients and forecast the occurrence of vasospasm.

The primary objective of this bachelor thesis, which involves evaluating the accuracy of AI-based segmentation tools in assigning the modified Fisher Score to aSAH patients and creating a novel method to predict the onset of vasospasm in affected individuals, has been effectively accomplished.

Aligning with the proposed secondary objectives (see 1.6.2.), the following conclusions are reached:

1. **Model Development:** An accurate U-Net segmentation model was trained for hemorrhage differentiation, achieving successfully Objective 1. This also enabled segment features measurements, such as hemorrhage volume, density, thickness and localization.
2. **Automated Scale:** The Random Forest classifier allowed the automatic assignment of the modified Fisher Scale with high accuracy, bearing significant clinical importance for aSAH patients management.
3. **Variability Assessment:** Interobserver variability between the two neuroradiologists demonstrated almost perfect agreement between them. Variability between the neuroradiologists and the AI-assigned scale presented moderate agreement, suggesting further refinement of the model.
4. **Predictive Evaluation:** Sensitivity and specificity values for vasospasm prediction showed similar performance between the manual-assigned scale and the AI-assigned scale.
5. **Extended Evaluation:** The logistic regression model's performance surpassed current used scales predictive values. This result validates the initial hypothesis that incorporating volumetric measurements and demographic variables can improve vasospasm prediction.

Overall, despite some limitations, this study establishes a robust base for future advancements in the management and prognostication of aSAH. The lack of reliable tools for predicting vasospasm remains a significant challenge within the healthcare system. To

address this issue, future research projects should focus on incorporating more sophisticated classification techniques, such as exploring deep learning approaches. Additionally, expanding the database to include patients from various institutions will enhance the generalizability and reliability of the findings. By doing so, these projects will pave the way for improved predictive tools and better patient outcomes in the management of aSAH.

## BIBLIOGRAPHY

- [1] Y. Li, L. Zhang, Q. Hu, H. Li, F. Jia, and J. Wu, “Automatic subarachnoid space segmentation and hemorrhage detection in clinical head CT scans,” *International Journal of Computer Assisted Radiology and Surgery*, vol. 7, no. 4, pp. 507–516, 2012, Epub 2011 Nov 12. doi: [10.1007/s11548-011-0664-3](https://doi.org/10.1007/s11548-011-0664-3).
- [2] M. Said *et al.*, “Subarachnoid hemorrhage early brain edema score (SEBES) as a radiographic marker of clinically relevant intracranial hypertension and unfavorable outcome after subarachnoid hemorrhage,” *European Journal of Neurology*, vol. 28, no. 12, pp. 4051–4059, 2021. doi: [10.1111/ene.15033](https://doi.org/10.1111/ene.15033).
- [3] J. Raymond, L. Létourneau-Guillon, and T. Darsaut, “Angiographic vasospasm and delayed cerebral ischemia after subarachnoid hemorrhage: Moving from theoretical to practical research pertinent to neurosurgical care,” *Neurochirurgie*, vol. 68, no. 4, pp. 363–366, 2022. doi: [10.1016/j.neuchi.2021.10.001](https://doi.org/10.1016/j.neuchi.2021.10.001).
- [4] M. Osgood, “Aneurysmal subarachnoid hemorrhage: Review of the pathophysiology and management strategies,” *Current Neurology and Neuroscience Reports*, vol. 21, no. 9, p. 50, 2021. doi: [10.1007/s11910-021-01136-9](https://doi.org/10.1007/s11910-021-01136-9).
- [5] B. Xu *et al.*, “CHSNet: Automatic lesion segmentation network guided by CT image features for acute cerebral hemorrhage,” *Computers in Biology and Medicine*, vol. 164, p. 107334, 2023, Epub 2023 Aug 9. doi: [10.1016/j.combiomed.2023.107334](https://doi.org/10.1016/j.combiomed.2023.107334).
- [6] E. Ziu, K. S. MZ, and F. Mesfin. “Subarachnoid hemorrhage.” Available from: StatPearls [Internet]. Treasure Island (FL): StatPearls Publishing; 2024 Jan-. (2023).
- [7] Cleveland Clinic. “Meninges.” Accessed: 04/04/2024. (2023), [Online]. Available: [%5Curl%7Bhttps://my.clevelandclinic.org/health/articles/22266-meninges%7D](https://my.clevelandclinic.org/health/articles/22266-meninges).
- [8] S. Nelson, I. Fragata, M. Rowland, and A. de Oliveira Manoel, “Editorial: Outcomes in subarachnoid hemorrhage,” *Frontiers in Neurology*, vol. 14, p. 1186473, 2023. doi: [10.3389/fneur.2023.1186473](https://doi.org/10.3389/fneur.2023.1186473).
- [9] P. L. R. García and D. R. García, “Hemorragia subaracnoidea: Epidemiología, etiología, fisiopatología y diagnóstico,” Spanish, *Revista Cubana de Neurología y Neurocirugía*, vol. 34, no. 1, pp. 1–12, Jan. 2024.
- [10] J. van Gijn, R. S. Kerr, and G. J. E. Rinkel, “Subarachnoid haemorrhage,” *Lancet*, vol. 369, pp. 306–318, 2007.
- [11] “Angioespasmo.” Accessed on 2024-05-09. (2024), [Online]. Available: <https://www.otorrinoweb.com/glosario/a/am-ap/2506-angioespasmo.html> (visited on 05/09/2024).

- [12] A. V. Ciurea, C. Palade, D. Voinescu, and D. A. Nica, “Subarachnoid hemorrhage and cerebral vasospasm - literature review,” *J Med Life*, vol. 6, no. 2, pp. 120–125, Jun. 2013.
- [13] C. Xia *et al.*, “Trends in the incidence of spontaneous subarachnoid hemorrhages in the United States, 2007-2017,” *Neurology*, vol. 100, no. 2, e123–e132, 2023. doi: [10.1212/WNL.00000000000201340](https://doi.org/10.1212/WNL.00000000000201340).
- [14] J. A. Frontera *et al.*, “Defining vasospasm after subarachnoid hemorrhage. What is the most clinically relevant definition?” *Stroke*, vol. 40, no. 6, pp. 1963–1968, 2009, Originally published 9 Apr 2009. doi: [10.1161/STROKEAHA.108.544700](https://doi.org/10.1161/STROKEAHA.108.544700). [Online]. Available: <https://doi.org/10.1161/STROKEAHA.108.544700>.
- [15] A. Y. Chan *et al.*, “Cerebral vasospasm after subarachnoid hemorrhage: Developing treatments,” *Brain Hemorrhages*, vol. 2, no. 1, pp. 15–23, 2021. doi: [10.1016/j.bhest.2020.08.003](https://doi.org/10.1016/j.bhest.2020.08.003). [Online]. Available: <https://www.sciencedirect.com/science/article/pii/S2589238X20300437>.
- [16] H. G. E. Nassar, A. A. Ghali, W. S. Bahnasy, and M. M. Elawady, “Vasospasm following aneurysmal subarachnoid hemorrhage: Prediction, detection, and intervention,” *Egypt J Neurol Psychiatr Neurosurg*, vol. 55, no. 1, p. 3, 2019. doi: [10.1186/s41983-018-0050-y](https://doi.org/10.1186/s41983-018-0050-y).
- [17] N. W. Dorsch, “Therapeutic approaches to vasospasm in subarachnoid hemorrhage,” *Curr Opin Crit Care*, vol. 8, no. 2, pp. 128–133, Apr. 2002. doi: [10.1097/00075198-200204000-00007](https://doi.org/10.1097/00075198-200204000-00007).
- [18] P. Lindvall, M. Runnerstam, R. Birgander, and L.-O. D. Koskinen, “The Fisher grading correlated to outcome in patients with subarachnoid haemorrhage,” *British Journal of Neurosurgery*, vol. 23, no. 2, pp. 188–192, 2009, Original Article.
- [19] C. G. Harrod, B. R. Bendok, and H. H. Batjer, “Prediction of cerebral vasospasm in patients presenting with aneurysmal subarachnoid hemorrhage: A review,” *Journal of Neurological Surgery*, 2005, Received February 19, 2004; Accepted January 7, 2005.
- [20] S. G. Keyrouz and M. N. Diringer, “Clinical review: Prevention and therapy of vasospasm in subarachnoid hemorrhage,” *Critical Care*, vol. 11, no. 4, p. 220, 2007. doi: [10.1186/cc5958](https://doi.org/10.1186/cc5958).
- [21] C. M. Sayama, J. K. Liu, and W. T. Couldwell, “Update on endovascular therapies for cerebral vasospasm induced by aneurysmal subarachnoid hemorrhage,” *Neurosurgical Focus*, vol. 21, no. 3, E12, Sep. 2006. doi: [10.3171/foc.2006.21.3.12](https://doi.org/10.3171/foc.2006.21.3.12).
- [22] L. M. Murillo-Bonilla, G. Magaña-Solano, and P. Uribe-Gonzalez, “Tratamiento del vasoespasmo cerebral en el paciente con hemorragia subaracnoidea aneurismática,” *Revista de Medicina Clínica*, vol. 2, no. 1, Jan. 2018.

- [23] W. E. Hunt and R. M. Hess, “Surgical risk as related to time of intervention in the repair of intracranial aneurysms,” *Journal of Neurosurgery*, vol. 28, pp. 14–20, 1968.
- [24] “Report of World Federation of Neurological Surgeons Committee on a Universal Subarachnoid Hemorrhage Grading Scale,” *Journal of Neurosurgery*, vol. 68, pp. 985–986, 1988.
- [25] C. M. Fisher, J. P. Kistler, and J. M. Davis, “Relation of cerebral vasospasm to subarachnoid hemorrhage visualized by computerized tomographic scanning,” *Neurosurgery*, vol. 6, no. 1, pp. 1–9, Jan. 1980. doi: [10.1227/00006123-198001000-00001](https://doi.org/10.1227/00006123-198001000-00001).
- [26] J. A. Frontera *et al.*, “Prediction of symptomatic vasospasm after subarachnoid hemorrhage: The modified Fisher scale,” *Neurosurgery*, vol. 59, no. 1, 21–27, discussion 21–27, Jul. 2006. doi: [10.1227/01.neu.0000243277.86222.6c](https://doi.org/10.1227/01.neu.0000243277.86222.6c).
- [27] F. Gaillard, H. Knipe, P. Fischer, *et al.*, *Fisher scale*, Reference article, Radiopaedia.org, Accessed on 21 Apr 2024, 2024. doi: [10.53347/rID-3877](https://doi.org/10.53347/rID-3877). [Online]. Available: <https://radiopaedia.org/articles/3877>.
- [28] D. Bhattarai, R. Sharma, F. Gaillard, *et al.*, *Modified Fisher scale*, Reference article, Radiopaedia.org, Accessed on 21 Apr 2024, 2024. doi: [10.53347/rID-41101](https://doi.org/10.53347/rID-41101). [Online]. Available: <https://radiopaedia.org/articles/41101>.
- [29] K. Yuan *et al.*, “Pre-operative predictors for post-operative pneumonia in aneurysmal subarachnoid hemorrhage after surgical clipping and endovascular coiling: A single-center retrospective study,” *Front. Neurol.*, vol. 13, p. 893516, 2022. doi: [10.3389/fneur.2022.893516](https://doi.org/10.3389/fneur.2022.893516).
- [30] Johns Hopkins Medicine. “Computed Tomography (CT Scan).” Accessed on 2024-05-08, Johns Hopkins Medicine. (2024), [Online]. Available: <https://www.hopkinsmedicine.org/health/treatment-tests-and-therapies/computed-tomography-ct-scan#:~:text=A%20CT%20scan%20is%20a%20diagnostic%20imaging%20procedure%20that%20uses,detailed%20than%20standard%20X%2Drays.> (visited on 05/08/2024).
- [31] National Institute of Biomedical Imaging and Bioengineering. “Computed tomography (CT).” Accessed on 2024-05-08, National Institute of Biomedical Imaging and Bioengineering. (2024), [Online]. Available: <https://www.nibib.nih.gov/science-education/science-topics/computed-tomography-ct> (visited on 05/08/2024).
- [32] A. A. Rabinstein, G. Lanzino, and E. F. M. Wijdicks, “Multidisciplinary management and emerging therapeutic strategies in aneurysmal subarachnoid haemorrhage,” *Lancet Neurology*, vol. 9, pp. 504–519, 2010.
- [33] J. I. Suarez, R. W. Tarr, and W. R. Selman, “Aneurysmal subarachnoid hemorrhage,” *New England Journal of Medicine*, vol. 354, pp. 387–396, 2006.

- [34] F. G. López, C. de la Linde Valverde, and F. P. Sánchez, “General management in intensive care of patient with spontaneous subarachnoid hemorrhage,” *Medicina Intensiva*, vol. 32, no. 7, Oct. 2008, Accessed on 2024-05-09. [Online]. Available: [https://scielo.isciii.es/scielo.php?script=sci\\_arttext&pid=S0210-56912008000700004](https://scielo.isciii.es/scielo.php?script=sci_arttext&pid=S0210-56912008000700004) (visited on 05/09/2024).
- [35] G. N. Hounsfield, “Computed medical imaging. Nobel lecture, december 8, 1979,” *Journal of Computer Assisted Tomography*, vol. 4, no. 5, pp. 665–674, 1980. doi: [10.1097/00004728-198010000-00017](https://doi.org/10.1097/00004728-198010000-00017).
- [36] K. Greenway, R. Sharma, and D. Vargas Carvajal, “Hounsfield unit,” *Radiopaedia.org*, 2024, Accessed on 27 May 2024. doi: [10.53347/rID-38181](https://doi.org/10.53347/rID-38181). [Online]. Available: <https://radiopaedia.org/articles/38181>.
- [37] M. Larobina, “Thirty years of the DICOM standard,” *Tomography*, vol. 9, no. 5, pp. 1829–1838, Oct. 2023. doi: [10.3390/tomography9050145](https://doi.org/10.3390/tomography9050145).
- [38] Radiopaedia, *Digital imaging and communications in medicine (DICOM)*, <https://radiopaedia.org/articles/digital-imaging-and-communications-in-medicine-dicom>, Accessed: 2024-05-12.
- [39] D. D. Patil and S. G. Deore, “Medical image segmentation: A review,” *International Journal of Computer Science and Mobile Computing*, vol. 2, no. 1, pp. 22–27, Jan. 2013.
- [40] F. Zhao and X. Xie, “An overview on interactive medical image segmentation,” *Annals of the BMVA*, vol. 2013, no. 7, pp. 1–22, 2013. doi: [10.1.1.413.2364](https://doi.org/10.1.1.413.2364). [Online]. Available: <http://dx.doi.org/doi=10.1.1.413.2364>.
- [41] S. Dubey and Y. Gupta, “Computational comparison of various existing edge detection techniques for medical images,” vol. 16, pp. 185–193, Jun. 2018.
- [42] J. Yuan *et al.*, “Automated quantification of compartmental blood volumes enables prediction of delayed cerebral ischemia and outcomes after aneurysmal subarachnoid hemorrhage,” *World Neurosurg*, vol. 170, e214–e222, Feb. 2023, Epub 2022 Oct 30. doi: [10.1016/j.wneu.2022.10.105](https://doi.org/10.1016/j.wneu.2022.10.105).
- [43] O. Ronneberger, P. Fischer, and T. Brox, “U-net: Convolutional networks for biomedical image segmentation,” in *Medical Image Computing and Computer-Assisted Intervention – MICCAI 2015*, N. Navab, J. Hornegger, W. M. Wells, and A. F. Frangi, Eds., ser. Lecture Notes in Computer Science, vol. 9351, Cham: Springer International Publishing, 2015, pp. 234–241. doi: [10.1007/978-3-319-24574-4\\_28](https://doi.org/10.1007/978-3-319-24574-4_28). [Online]. Available: <http://lmb.informatik.uni-freiburg.de/people/ronneber/u-net>.

- [44] A. S. Dumont and H. K. Yeoh, “Predicting symptomatic cerebral vasospasm after aneurysmal subarachnoid hemorrhage: Are we there yet?” *World Neurosurgery*, vol. 75, pp. 57–63, 2011, Commentary on: Prediction of Symptomatic Cerebral Vasospasm after Aneurysmal Subarachnoid Hemorrhage with an Artificial Neural Network: Feasibility and Comparison with Logistic Regression Models by Dumont et al.
- [45] T. Takemae, M. Mizukami, H. Kin, T. Kawase, and G. Araki, “Computed tomography of ruptured intracranial aneurysms in acute stage—relationship between vasospasm and high density on CT scan (author’s transl),” *No To Shinkei*, vol. 30, pp. 861–866, 1978, [in Japanese].
- [46] A. Hijdra, P. J. Brouwers, M. Vermeulen, and J. van Gijn, “Grading the amount of blood on computed tomograms after subarachnoid hemorrhage.,” *Stroke*, vol. 21, no. 8, pp. 1156–1161, 1990. doi: [10.1161/01.STR.21.8.1156](https://doi.org/10.1161/01.STR.21.8.1156). eprint: <https://www.ahajournals.org/doi/pdf/10.1161/01.STR.21.8.1156>. [Online]. Available: <https://www.ahajournals.org/doi/abs/10.1161/01.STR.21.8.1156>.
- [47] M. Said *et al.*, “Comparing radiographic scores for prediction of complications and outcome of aneurysmal subarachnoid hemorrhage: Which performs best?” *European Journal of Neurology*, vol. 30, no. 3, pp. 659–670, Mar. 2023. doi: [10.1111/ene.15634](https://doi.org/10.1111/ene.15634). eprint: [2022Nov29](https://doi.org/2022Nov29).
- [48] N. O. Souza *et al.*, “The role of vasograde as a simple grading scale to predict delayed cerebral ischemia and functional outcome after aneurysmal subarachnoid hemorrhage,” *Neurocritical Care*, vol. 38, no. 1, pp. 96–104, Feb. 2023. doi: [10.1007/s12028-022-01577-1](https://doi.org/10.1007/s12028-022-01577-1). eprint: [2022Aug24](https://doi.org/2022Aug24).
- [49] J. Claassen, G. Bernardini, K. Kreiter, J. Bates, Y. Du, D. Copeland, *et al.*, “Effect of cisternal and ventricular blood on risk of delayed cerebral ischemia after subarachnoid hemorrhage: The Fisher scale revisited,” *Stroke*, vol. 32, pp. 201–220, 2001.
- [50] A. Kramer *et al.*, “A comparison of 3 radiographic scales for the prediction of delayed ischemia and prognosis following subarachnoid hemorrhage,” *Journal of Neurosurgery*, vol. 109, pp. 199–207, 2008. doi: [10.3171/JNS/2008/109/8/0199](https://doi.org/10.3171/JNS/2008/109/8/0199).
- [51] B. Weir, G. Kongable, N. Kassell, J. Schultz, L. Truskowski, and A. Sigrest, “Cigarette smoking as a cause of aneurysmal subarachnoid hemorrhage and risk for vasospasm: A report of the cooperative aneurysm study,” *Journal of Neurosurgery*, vol. 89, pp. 405–411, 1998. doi: [10.3171/jns.1998.89.3.0405](https://doi.org/10.3171/jns.1998.89.3.0405).
- [52] A. Qureshi, G. Sung, A. Razumovsky, K. Lane, R. Straw, and J. Ulatowski, “Early identification of patients at risk for symptomatic vasospasm after aneurysmal subarachnoid hemorrhage,” *Critical Care Medicine*, vol. 28, pp. 984–990, 2000.

- [53] K. Basu, R. Sinha, A. Ong, and T. Basu, “Artificial intelligence: How is it changing medical sciences and its future?” *Indian Journal of Dermatology*, vol. 65, no. 5, pp. 365–370, Sep. 2020. doi: [10.4103/ijd.IJD\\_421\\_20](https://doi.org/10.4103/ijd.IJD_421_20).
- [54] J. Skoch, R. Tahir, T. Abruzzo, J. M. Taylor, M. Zuccarello, and S. Vadivelu, “Predicting symptomatic cerebral vasospasm after aneurysmal subarachnoid hemorrhage with an artificial neural network in a pediatric population,” *Child’s Nervous System*, vol. 33, no. 12, pp. 2153–2157, 2017. doi: [10.1007/s00381-017-3573-0](https://doi.org/10.1007/s00381-017-3573-0).
- [55] T. M. Dumont, A. I. Rughani, and B. I. Tranmer, “Prediction of symptomatic cerebral vasospasm after aneurysmal subarachnoid hemorrhage with an artificial neural network: Feasibility and comparison with logistic regression models,” *World Neurosurgery*, vol. 75, no. 1, pp. 57–63, 2011. doi: [10.1016/j.wneu.2010.07.007](https://doi.org/10.1016/j.wneu.2010.07.007).
- [56] J. P. Savarraj *et al.*, “Machine learning to predict delayed cerebral ischemia and outcomes in subarachnoid hemorrhage,” *Neurology*, vol. 96, no. e553-e562, 2021. doi: [10.1212/WNL.00000000000011211](https://doi.org/10.1212/WNL.00000000000011211).
- [57] L. A. Ramos *et al.*, “Machine learning improves prediction of delayed cerebral ischemia in patients with subarachnoid hemorrhage,” *Journal of NeuroInterventional Surgery*, vol. 11, pp. 497–502, 2018. doi: [10.1136/neurintsurg-2018-014258](https://doi.org/10.1136/neurintsurg-2018-014258).
- [58] A. Thaniellis *et al.*, “Development and external validation of a deep learning algorithm to identify and localize subarachnoid hemorrhage on ct scans,” *Neurology*, vol. 100, e1257–e1266, 2023, © 2023 The Author(s). Published by Wolters Kluwer Health, Inc. on behalf of the American Academy of Neurology. doi: [10.1212/WNL.000000000000201710](https://doi.org/10.1212/WNL.000000000000201710).
- [59] G. Danala *et al.*, “Applying quantitative radiographic image markers to predict clinical complications after aneurysmal subarachnoid hemorrhage: A pilot study,” *Annals of Biomedical Engineering*, vol. 50, no. 4, pp. 413–425, 2022. doi: [10.1007/s10439-022-02926-z](https://doi.org/10.1007/s10439-022-02926-z).
- [60] Python Software Foundation, *Python*, Accessed: 2024-05-27, 2024. [Online]. Available: <https://www.python.org>.
- [61] Spyder Development Team, *Spyder ide*, Accessed: 2024-05-27, 2024. [Online]. Available: <https://www.spyder-ide.org>.
- [62] 3D Slicer Community, *3D slicer*, Accessed: 2024-05-27, 2024. [Online]. Available: <https://www.slicer.org>.
- [63] D. Riehle, D. Reiser, and H. W. Griepentrog, “Robust index-based semantic plant/background segmentation for RGB-images,” *Computers and Electronics in Agriculture*, vol. 169, p. 105201, 2020. doi: [10.1016/j.compag.2019.105201](https://doi.org/10.1016/j.compag.2019.105201). [Online]. Available: <https://www.sciencedirect.com/science/article/pii/S016816991931420X>.

- [64] SVI, *Image histogram*, Accessed: 2024-05-27, 2024. [Online]. Available: <https://svi.nl/ImageHistogram#:~:text=An%20image%20histogram%20is%20a,a%20certain%20intensity%20value%20range>.
- [65] P. M. Contributors, *Project MONAI*, <https://monai.io/index.html>, Accessed: 2024-05-27, 2024.
- [66] A. Myronenko, “3D MRI brain tumor segmentation using autoencoder regularization,” in *International MICCAI Brainlesion Workshop*, Springer, Cham, 2018. [Online]. Available: <https://arxiv.org/abs/1810.11654>.
- [67] A. N. Md Sakib, N. Anjum, and S. M. M. Ahsan, “Segmentation of hemorrhagic areas in human brain from CT scan images,” in *2022 4th International Conference on Sustainable Technologies for Industry 4.0 (STI)*, Dhaka, Bangladesh, 2022, pp. 1–5. doi: [10.1109/STI56238.2022.10103333](https://doi.org/10.1109/STI56238.2022.10103333).
- [68] F. C. Kitamura, *Head CT - hemorrhage*, 2018. doi: [10.34740/KAGGLE/DSV/152137](https://doi.org/10.34740/KAGGLE/DSV/152137). [Online]. Available: <https://www.kaggle.com/dsv/152137>.
- [69] *Region growing*, <https://cloudinary.com/glossary/region-growing>, Accessed: 2024-05-27, Cloudinary. [Online]. Available: <https://cloudinary.com/glossary/region-growing#:~:text=Region%20Growing%20is%20an%20image,that%20meet%20specific%20similarity%20conditions>.
- [70] J. Wasserthal, M. Meyer, H.-C. H. Breit, J. Cyriac, Y. Shan, and M. Segeroth, “Totalsegmentator: Robust segmentation of 104 anatomical structures in CT images,” *arXiv preprint arXiv:2208.05868*, 2022. [Online]. Available: <https://arxiv.org/abs/2208.05868>.
- [71] F. Isensee, P. F. Jaeger, S. A. A. Kohl, J. Petersen, and K. H. Maier-Hein, “NnUNet: A self-configuring method for deep learning-based biomedical image segmentation,” *Nature Methods*, vol. 18, no. 2, pp. 203–211, 2021.
- [72] P. Inkeaw *et al.*, “Automatic hemorrhage segmentation on head CT scan for traumatic brain injury using 3d deep learning model,” *Computers in Biology and Medicine*, vol. 146, p. 105 530, 2022. doi: <https://doi.org/10.1016/j.compbiomed.2022.105530>. [Online]. Available: <https://www.sciencedirect.com/science/article/pii/S0010482522003225>.
- [73] M. Nijati *et al.*, “A symmetric prior knowledge based deep learning model for intracerebral hemorrhage lesion segmentation,” *Frontiers in Physiology*, vol. 13, p. 977 427, Nov. 2022. doi: [10.3389/fphys.2022.977427](https://doi.org/10.3389/fphys.2022.977427).
- [74] Instituto Nacional de Estadística (INE), <https://www.ine.es>, Accessed: 2024-06-03.
- [75] iDoctor, *Precio de un tac barato por privado*, Accessed: 2024-06-05, n.d. [Online]. Available: <https://idocotor.es/blog/precio-de-un-tac-barato-por-privado/>.